

SEARCHING FOR NEW PHYSICS IN $b \rightarrow s\ell^+\ell^-$ TRANSITIONS AT THE LHCb EXPERIMENT

L. Pescatore

*Thesis submitted for the degree of
Doctor of Philosophy*



Particle Physics Group,
School of Physics and Astronomy,
University of Birmingham.

September 11, 2015

Contents

1	Introduction	1
1.1	The electroweak interaction	4
1.2	Flavour and the CKM matrix	5
1.3	The puzzles of the SM	9
1.3.1	The flavour problem	10
1.4	Beyond the Standard Model	11
1.4.1	Flavour and BSM theories	11
1.5	Rare decays: a tool to search for new physics	13
1.5.1	Theoretical framework: the effective Hamiltonian	14
1.5.2	Operators	16
1.5.3	Phenomenology of $b \rightarrow s\ell^+\ell^-$ decays	18
1.5.4	Observables in $b \rightarrow s\ell^+\ell^-$ decays	19
1.6	Experimental status	20
1.6.1	Dimuon decays of b hadrons	20
1.6.2	Semileptonic $b \rightarrow s\ell^+\ell^-$ decays of b hadrons	22
1.6.3	Lepton Flavour Violation searches	23
2	The LHCb detector at the Large Hadron Collider	25
2.1	The Large Hadron Collider	25
2.2	The LHCb detector	27
2.3	The magnet	29
2.4	Tracking system	29
2.5	Calorimeters	32
2.5.1	Bremsstrahlung recovery for electrons	34
2.6	RICH	35
2.7	The muon system	36
2.8	Particle identification	37
2.8.1	PID calibration	39
2.9	Trigger and software	39
2.10	Kinematical fits	41
2.11	Validation of hadronic processes in the simulation	42
2.11.1	Geometry and interaction probability	44
2.11.2	PDG prediction	45
2.11.3	Validation results	46
2.12	Material budget studies	49
A	Extra	57

A.0.1	Quantum Electrodynamics: an example of gauge field theory	57
A.1	Anomalies	58

¹

CHAPTER 1

²

³

Introduction

⁴

⁵ The Standard Model of particle physics (SM) is a Quantum Field Theory (QFT)
⁶ describing strong and electroweak (EW) interactions. It was formulated in his cur-
⁷ rent form in the mid-70s and has been an extremely successful and predictive theory
⁸ since then. Almost all known phenomena from 1 eV up to several hundred GeV are
⁹ well described by the SM and experiments at the Large Hadron Collider (LHC) are
¹⁰ now probing the SM up to and above the TeV scale. As an example of the level
¹¹ of accuracy of the SM, Tab. 1.1 reports the predicted and measured values of the
¹² widths of the Z and W bosons [1]. Finally, in 2013 the Higgs boson was observed,
¹³ one of the fundamental building blocks of the theory, which gives a solid basis to it
¹⁴ by introducing a mechanism that produces particles' masses [2]. Despite the suc-
¹⁵ cess of the SM, experimentally well established effects, like neutrino oscillations and
¹⁶ the presence of dark matter, are outside the reach of this theory. Furthermore, the
¹⁷ model does not include the description of gravity, which can be neglected at the EW
¹⁸ energy scale. Therefore this motivates the search for New Physics (NP).

Table 1.1: Predicted and measured values of the decay widths of the Z and W bosons.

Quantity	Predicted	Measured
Γ_Z	2.4960 ± 0.0002 GeV	2.4952 ± 0.0023 GeV
Γ_W	2.0915 ± 0.0005 GeV	2.085 ± 0.042 GeV

The SM is based on the symmetry groups of strong, $SU(3)_C$, and electroweak, $SU(2)_W \times U(1)_Y$, interactions. The subscripts C, W and Y stand for colour charge, weak isospin and hyper-charge respectively. The Lagrangian describing the SM results from the application of the principle of invariance under the unitary group given by the product $SU(3)_C \times SU(2)_W \times U(1)_Y$, which reflects conservation laws such as the conservation of electric and strong charge. The model has then 26 free parameters, which are experimentally measured.

Particles included in the SM can be grouped under a few categories depending on their properties and ability to interact with each other. The first distinction is between fermions, half-integer spin particles, and bosons, integer spin particles. Fermions constitute the basic building blocks of matter, while bosons are the mediators of the interactions. Since the concept of bosonic mediators of interactions arises because of gauge symmetry [3], they are called “gauge bosons”. The list of the

Table 1.2: Fundamental forces of nature together with their gauge bosons, relative strengths and range. Gravity is not included in the SM and the graviton is hypothetical at the current time.

Interaction	Mediator	Rel. strength	Range (m)	Mediator mass (GeV/c^2)
Strong	g	1	∞	0
EM	γ	10^{-3}	∞	0
Weak	Z, W^\pm	10^{-16}	10^{-18}	$W^\pm = 80.399$ $Z_0 = 91.188$
Gravity	g^0 (graviton?)	10^{-41}	∞	0

known interactions with their force carrier and properties is reported in Tab. 1.2. The matter of which we are made of is mainly composed of electrons and protons, which have spin 1/2; protons are in turn composed of u and d quarks, which again have spin 1/2. Among fermions one can then consider two smaller groups: quarks and leptons. Quarks carry colour charge and therefore can interact through the,

³⁷ so called, strong interaction, while leptons, which do not carry colour charge, are
³⁸ insensitive to it. For each particle a corresponding anti-particle exists with opposite
³⁹ quantum numbers. Finally, fermions are divided into three families having similar
⁴⁰ properties but different masses. This last structure embedded in the SM is also
⁴¹ called “flavour structure” and it will be the main tool used in this thesis; a more
⁴² detailed description of it is given in the next sections. A schematic view of the fundamental particles in the SM is shown in Fig. 1.1. Due to the asymptotic freedom

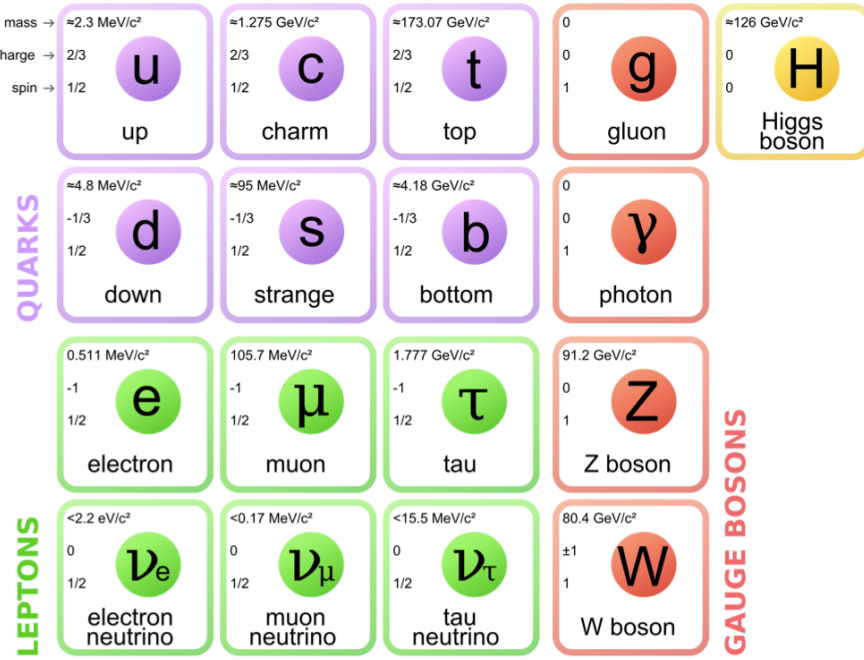


Figure 1.1: A scheme of the fundamental particles in the SM with their properties.

⁴³

⁴⁴ of the strong interaction quarks cannot be observed alone but are always combined
⁴⁵ with other quarks to form color singlets. Non-fundamental particles composed by
⁴⁶ quarks are called hadrons and can be divided in mesons, where the color singlet is
⁴⁷ achieved by the combination of a quark and its antiquark ($q \bar{q}$), and baryons formed
⁴⁸ by three quarks ($q q q$) of different colours. Recently, in 2014 and 2015 evidence for
⁴⁹ new states, formed by four and five quarks, was found [4, 5].

50 1.1 The electroweak interaction

51 The electromagnetic interaction is responsible for binding electrons and nuclei to-
52 gether in atoms and its mediator is the photon. The weak interaction is responsible
53 for the β decay of nuclei and is mediated by the emission or absorption of W^\pm and
54 Z bosons. Unlike the electromagnetic force, that affects only charged particles, all
55 known fermions interact through the weak interaction. The weak interaction is also
56 the only one that violates the parity symmetry, which states that interactions are
57 invariant under a reflection of all coordinates. This symmetry breaking arises from
58 the fact that only left-handed fermions interact through the weak interaction as dis-
59 covered by Wu in 1957 [6]. Similarly, the weak interaction is the only one that also
60 breaks the CP symmetry, which combines parity transformations and charge conju-
61 gation. This is particularly interesting because all interactions are invariant under
62 the CPT transformation, which combines the CP transformation and time reversal,
63 hence, breaking CP the weak interaction must also be not invariant under time re-
64 versal. In 1968 Salam, Glashow and Weinberg unified the weak and electromagnetic
65 forces in a single theory, where the coupling constants of the electromagnetic, e ,
66 and weak, g , interactions are linked by the weak mixing angle, θ_W by the relation
67 $g \sin \theta_W = e$ [1]. The electroweak symmetry is spontaneously broken by the Higgs
68 field [7] and this causes the W^\pm and Z bosons to become massive (see Tab. 1.2)
69 and consequently the weak force has a very short range. In fact using Heisenberg's
70 Principle ($\Delta E \Delta t > \hbar$) together with Einstein's formula $\Delta E = mc^2$, which relates
71 mass and energy, and knowing that the maximum space that a particle can cover
72 in a time Δt is $r = c\Delta t$, qualitatively $r \sim \hbar/mc$. In this picture the carriers of the
73 weak force can travel $r \sim 2 \cdot 10^{-3}$ fm. The photon must instead be massless in the
74 theory, which accounts for the long range of the electromagnetic force. The EW
75 interactions are divided into charged currents (CC) and neutral currents (NC). In
76 the first group, quarks and leptons interact with the W^\pm bosons, producing decays
77 such as $\mu^+(\mu^-) \rightarrow e^+ \nu_e \bar{\nu}_\mu (e^- \bar{\nu}_e \nu_\mu)$ and $n \rightarrow p e^- \bar{\nu}_e (\bar{p} e^+ \nu_e)$. The study of these pro-
78 cesses confirmed that only the left-handed (right-handed) component of fermions
79 (anti-fermions) takes part in weak processes. The CC interactions have a peculiar-

80 ity: they are the only interactions in the SM that violate flavour conservation at
81 tree level (see next section), while any other interaction not conserving flavour has
82 to happen through loops. The second group of EW interactions, NC, corresponds
83 to diagrams mediated by a photon or a Z boson interacting with a fermion and its
84 anti-fermion.

85 1.2 Flavour and the CKM matrix

86 “Flavour” in particle physics refers to the quark-lepton composition of a particle.
87 The introduction of flavour quantum numbers was motivated in order to explain
88 why some decays, although kinematically allowed, had never been observed. To all
89 leptons is assigned a quantum number $L_\ell = 1$ (where $\ell = e, \mu, \tau$), which in the SM is
90 conserved by all interactions. This conservation is experimentally well established;
91 for example decays like $\mu^- \rightarrow e^- \gamma$ have never been observed. This is explained by
92 the fact that the lepton number in the initial and final state are different and the
93 decay would violate lepton flavour. In the hadronic sector particles carry flavour
94 numbers described as follow:

- 95 • *Isospin*: $I_3 = 1/2$ for the up quark and $I_3 = -1/2$ for the down quark;
- 96 • *Strangeness*: $S = -(n_s - \bar{n}_s)$, where n_s and \bar{n}_s are the numbers of strange and
97 anti-strange quarks respectively;
- 98 • *charmness, bottomness, topness*: in analogy to strangeness they are respec-
99 tively defined as $C = -(n_c - \bar{n}_c)$, $B = -(n_b - \bar{n}_b)$, $T = -(n_t - \bar{n}_t)$.

100 As mentioned before, in the SM the only interaction violating flavour conservation
101 is the weak interaction when mediated by W^\pm bosons.

102 Measuring branching fractions of weak decays like $\pi \rightarrow \mu\nu_\mu$ and $K \rightarrow \mu\nu_\mu$, corre-
103 sponding respectively to $ud \rightarrow \mu\nu_\mu$ and $us \rightarrow \mu\nu_\mu$ processes, suggested the existence
104 of more than one coupling constant for different quarks. Nicola Cabibbo [1], in order

to preserve the universality of weak interactions, suggested that the branching fraction differences could arise from the fact that the doublets participating in the weak interactions are an admixture of the flavour eigenstates. He therefore introduced the Cabibbo angle, θ_c , considering that eigenstates participating to the weak interaction are rotated with respect of the flavour eigenstates.

$$\begin{pmatrix} d_W \\ s_W \end{pmatrix} = \begin{pmatrix} \cos \theta_c & \sin \theta_c \\ -\sin \theta_c & \cos \theta_c \end{pmatrix} \begin{pmatrix} d \\ s \end{pmatrix} = \begin{pmatrix} \cos \theta_c \cdot d + \sin \theta_c \cdot s \\ \cos \theta_c \cdot s - \sin \theta_c \cdot d \end{pmatrix} \quad (1.1)$$

Considering a 6 quark system one angle is not enough to describe a rotation but the mixing can be generalised using a 3×3 unitary matrix, which is called CKM matrix, from the names of Cabibbo, Kobayashi and Maskawa. The unitarity of the matrix is required to preserve the universality of the weak interaction. Theoretically, a $N \times N$ complex matrix depends on $2 \cdot N^2$ real parameters. Requiring unitarity ($AA^\dagger = A(A^*)^T = I$), the number of independent parameters left is $(N - 1)^2$. Therefore a 3×3 matrix depends then on 4 real parameters, which can be divided in 3 real constants and one imaginary phase. The imaginary phase generates the CP-violation which was observed in weak interactions. Equation 1.2 reports a parametrisation of

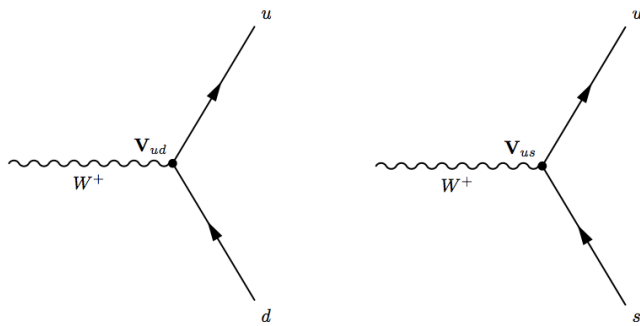


Figure 1.2: Feynman diagrams with CKM weights on weak interaction vertices

the CKM matrix together with the most recent measured values of its elements [1]. In this parametrisation ρ , A , and λ are the real constants and η the imaginary phase

and Eq. 1.3 shows their relations with the 3 mixing angles.

$$V_{CKM} = \begin{pmatrix} 1 - \lambda^2/2 & \lambda & A\lambda^3(\rho - i\eta) \\ -\lambda & 1 - \lambda^2/2 & A\lambda^2 \\ A\lambda^3(1 - \rho - i\eta) & A\lambda^2 & 1 \end{pmatrix} + O(\lambda^3) = \\ = \begin{pmatrix} 0.97427 \pm 0.00015 & 0.22534 \pm 0.00065 & 0.00351^{+0.00015}_{-0.0014} \\ 0.22520 \pm 0.00065 & 0.97344 \pm 0.00016 & 0.00412^{+0.0011}_{-0.0005} \\ 0.00867^{+0.00029}_{-0.00031} & 0.0404^{+0.0011}_{-0.0005} & 0.999146^{+0.000021}_{-0.000046} \end{pmatrix} \quad (1.2)$$

110

$$\begin{aligned} \lambda &= \sin(\theta_{12}) = \sin(\theta_c) \\ A\lambda^2 &= \sin(\theta_{23}) \\ A\lambda^3(\rho - i\eta) &= \sin(\theta_{13})e^{i\delta} \end{aligned} \quad (1.3)$$

111 Figure 1.2 displays examples of CC processes together with the CKM elements
 112 associated with their vertices. It is interesting to note that the CKM matrix has a
 113 hierarchical form, namely elements on the diagonal are approximately 1 and become
 114 smaller and smaller going farther from the diagonal. This structure is not explained
 115 in the SM. Another feature to note is that, due to the unitarity of the matrix, the
 116 transformation has no effect on neutral interactions. In fact defining $q' = Vq$:

$$\bar{q}'q' = \bar{q}V^*Vq = \bar{q}q. \quad (1.4)$$

117 The unitarity of the CKM matrix imposes constraints to its elements of the form:

$$\sum_i |V_{ik}|^2 = 1 \text{ and } \sum_k V_{ik}V_{jk}^* = 0. \quad (1.5)$$

118 These correspond to constraints to three complex numbers, which can be viewed
 119 as the sides of triangles in the (ρ, η) plane; these are called “unitarity triangles”.
 120 The most commonly used unitarity triangle arises from $V_{ud}V_{ub}^* + V_{cd}V_{cb}^* + V_{td}V_{tb}^* = 0$.
 121 Figure 1.3 shows a representation of such triangle together with a plot summarising
 122 the most up to date experimental constraints to its parameters [8]. The precise
 123 measurement of the parameters of the CKM matrix is a powerful stability test of

¹²⁴ the SM and sets a solid base for new physics searches in the flavour sector. One of
¹²⁵ the main goals of the LHCb experiment is to precisely measure the angle γ , which
is currently the least constrained by measurements.

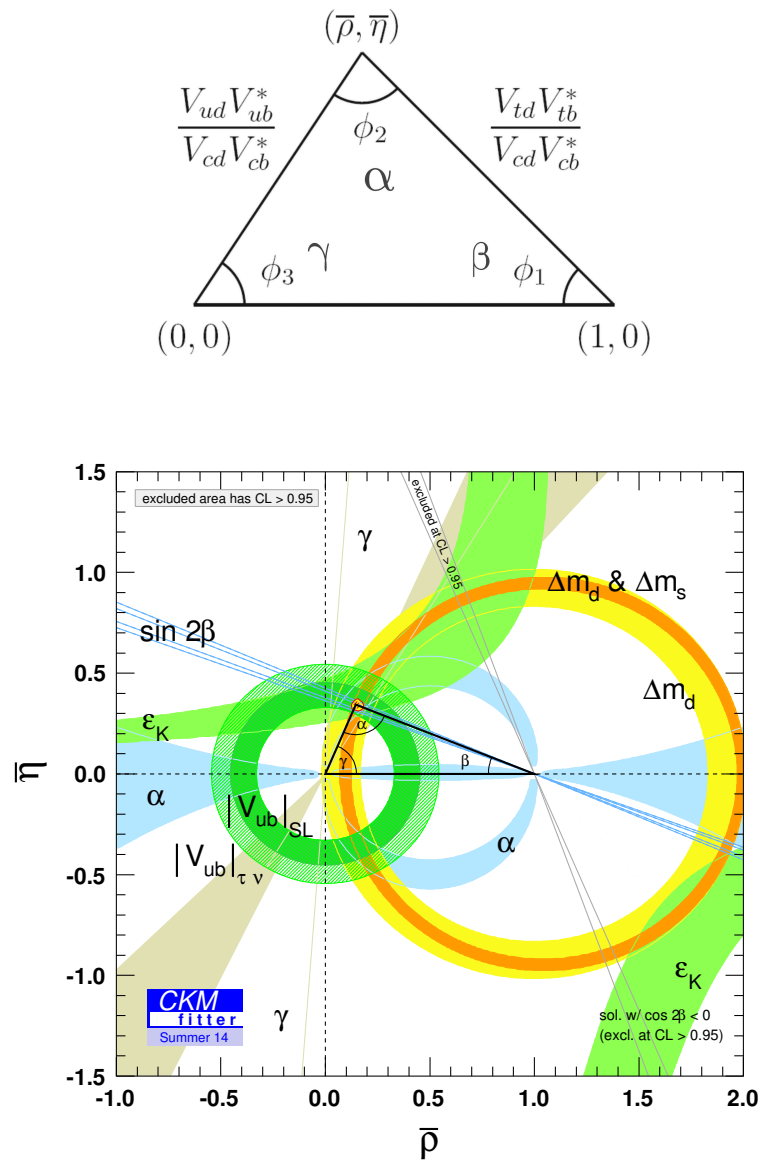


Figure 1.3: (top) A representation of the unitarity triangle and its parameters. (bottom) A summary of the most up to date measurements of the unitarity triangle parameters [8].

127 1.3 The puzzles of the SM

128 Despite the confirmation of many predictions of the SM, the theory has several
129 limitations and is unable to account for some well established experimental facts:

130 • *Dark matter*: experimental evidence tells us that the content of visible matter
131 in the universe is not enough to account for the observed rotation of galaxies [9].
132 The most natural way to solve the problem is the hypothesis of a form of
133 matter that interacts with the gravitational field but not with the other SM
134 interactions.

135 • *Matter-antimatter asymmetry*: a large asymmetry is observed between the
136 quantity of matter and antimatter in the universe, $O(10^{-9})$. Assuming that
137 both were equally created in the initial state of the universe, a condition such
138 as the violation of the CP symmetry is necessary to account for the observed
139 imbalance. However, the magnitude of CP violation predicted by the SM,
140 $O(10^{-20})$, is not enough to explain the observed imbalance [10].

141 • *Gravity*: even though the gravitational force was the first to be discovered this
142 is not included in the SM. When introducing gravity in the framework of QFT
143 the theory diverges. On the other hand gravity becomes irrelevant for small
144 masses as those of particles and can be neglected in good approximation at the
145 EW energy scale. Many attempts were made but there is not yet a consistent
146 procedure to introduce gravity in the SM.

147 • *Neutrino oscillation*: measurements regarding solar and atmospheric neutrinos
148 as wells as neutrinos from nuclear reactors established that neutrinos can
149 change flavour while propagating in space. This is not predicted in the SM, in
150 fact in the SM neutrinos are massless, while an oscillation requires a non zero
151 mass [11, 12, 13, 14].

152 • *The hierarchy problem*: the mass of a scalar (spin 0) particle, such as the
153 Higgs boson, suffers from quantum corrections due to the physics at high

¹⁵⁴ energy scales. As new physics can appear anywhere up to the Planck scale,
¹⁵⁵ $\sim 10^{19}$ GeV, at which gravity cannot be neglected any more, these corrections
¹⁵⁶ can be very large and it would require a high level of fine-tuning for them to
¹⁵⁷ cancel out and give such a small value as the one measured for the Higgs Mass,
¹⁵⁸ ~ 126 GeV/ c^2 [15, 16].

¹⁵⁹ In conclusion, even though the SM has been very successful in describing the prop-
¹⁶⁰ erties of the observed particles and their interactions so far, because of its many
¹⁶¹ puzzles, it is believed only to be part of a more general theory or only to be valid
¹⁶² up to a certain energy scale.

¹⁶³ 1.3.1 The flavour problem

¹⁶⁴ Flavour Changing Charged Currents (FCCC) that are mediated by the W^\pm bosons
¹⁶⁵ are the only sources of flavour changing interaction in the SM and, in particular, of
¹⁶⁶ generation changing interactions, where a quark or a lepton of a family transforms
¹⁶⁷ into one of another family. Another class of processes is the Flavour Changing
¹⁶⁸ Neutral Currents (FCNCs), e.g. transitions from a b quark with a charge of $-1/3$ to
¹⁶⁹ a s or d quark with the same charge. Examples of FCNC transitions in the quark
 and lepton sector are shown in Fig. 1.4. In the SM there is no fundamental reason

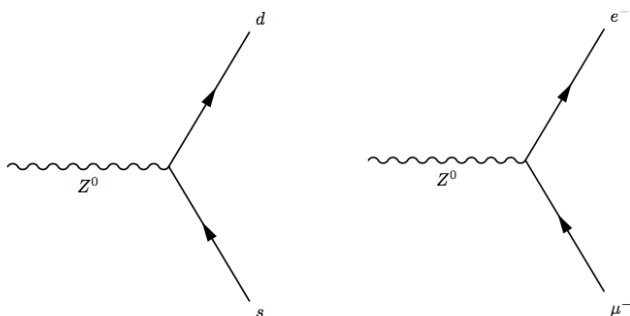


Figure 1.4: Feynman diagrams of FCNCs processes forbidden in the SM.

¹⁷⁰
¹⁷¹ why there cannot be FCNCs and, yet, they are experimentally observed to be highly
¹⁷² suppressed. On the other hand the observation of neutrino oscillation proves that

flavour is not an exact symmetry and is not always conserved. Furthermore, the values of the terms of the CKM matrix and the PMNS matrix, which the mixing-matrix, equivalent to the CKM, in the lepton sector, are not explained in the SM and have to be measured experimentally. These open problems motivate searches for flavour symmetries and deeper motivations for flavour conservation.

1.4 Beyond the Standard Model

From the last sections it is evident that, despite the great success of the SM, there is a need to explore theories Beyond the SM (BSM). Among the most promising approaches there are those involving Super-Symmetry and extra-dimensions. In Super-Symmetry new degrees of freedom are introduced to suppress the diverging terms of the scalar mass. This theory assumes that for each fermion there is a corresponding boson and, since bosons and fermions contribute with opposite sign to the mass term, these would naturally cancel out [17]. Supersymmetry also provides a candidate for dark matter, the neutralino, which is a weakly interacting stable particle. The idea to introduce extra-dimensions was triggered by the fact that, normally, gravity is not relevant in particle physics but it would be natural if all forces had similar strength. By adding extra dimensions to the normal 3 spatial dimensions, one can restore the strength of gravity, as this could be dispersed by the wider space available [18]. In all these approaches severe constraints to masses and couplings must be imposed to maintain compatibility with the SM at the electroweak scale.

1.4.1 Flavour and BSM theories

Most BSM theories predict processes violating flavour conservation. Therefore, the observation or non-observation of these processes can give important information about new physics. BSM theories can be classified according to the amount of flavour

violation they introduce. The first class of models to consider is those with Minimal Flavour Violation (MFV). These are models in which the only sources of flavour changing transitions are governed by the CKM matrix and the CKM phase is the only source of CP violation. These features can be assured by symmetry principles, which makes these types of models naturally compatible with the SM. Examples of such models include the MSSM with minimal flavour violation and the SM with one extra-dimension. Reviews of MFV models are presented in Refs. [19, 20]. The MFV paradigm provides a way to resolve the tension between expectation, driven by naturalness arguments, that NP should be at the TeV scale and limits on FCNC processes that point to much higher scales. A powerful test of MFV is provided by the study of ratios between $b \rightarrow d$ and $b \rightarrow s$ transitions, because their hamiltonians share the same structure. One particularly important example is the ratio of B^0 and B_s^0 dimuon decay rates [21], as this is a purely leptonic decay free from hadronic uncertainties. In the SM such ratios are approximately equal to $|V_{td}/V_{ts}| \sim 1/25$, only modified by phase space and hadronic matrix elements, while they can take very different values in non-MFV models.

In the quest for new physics an important role is also played by simplified models as an intermediate model building step. Instead of constructing models valid up to the GUT scale one can consider simplified models, where the SM is extended incorporating a new sector with a limited number of parameters. Such models are easier to constrain but can nevertheless point in the right direction to build more complete theories. The choice of the new sector to add can be driven by the need to explain existing tensions between data and SM predictions or by theoretical prejudice. Two models especially relevant when studying rare decays, which are the main topic of this thesis, are Z'-penguins and leptoquarks. A Z'-penguin is a FCNC process involving a neutral field arising from an extra U(1) gauge symmetry. As for the SM penguins, this field contributes in loops causing modifications of the effective couplings with respect to the SM. A survey of Z' models can be found in Ref. [22]. Leptoquarks are bosonic particles that carry both quark and lepton flavour quantum numbers. For simplicity they are commonly assumed to be scalar particles.

228 A tree level exchange of a leptoquark induces processes such as $b \rightarrow (s, d)\ell^+\ell^-$, and
229 therefore can result in an enhancement of their decay rates with respect to the
230 SM [23]. Leptoquarks would also provide a natural explanation for non-universal
231 couplings to leptons.

232 1.5 Rare decays: a tool to search for new physics

233 In the Standard Model FCNC processes are forbidden at tree level but can occur
234 through loop diagrams such as penguin or W box diagrams (see Fig. 1.5). The branching
235 fractions of decays going through these processes are small, typically $\sim 10^{-6}$ or
236 lower, and therefore they are called “rare decays”. Additional contributions to the
237 virtual loops are not necessarily suppressed with respect to the SM component and
238 this makes these decays very sensitive to new physics. This approach to new physics
239 searches is interesting as new particles could be at high mass scales not accessible at
240 colliders but their effect could be observed in loops. Radiative and penguin decays
241 are particularly interesting because they are theoretically well understood, which
242 allows precise comparisons with measurements. Furthermore, they provide a great
243 quantity of observables that can be affected by new physics, not only decay rates,
244 but also CP asymmetries and angular observables such as forward-backward asym-
245 metries. The joint analysis of different observables can help building a consistent
 picture and rule out specific models.

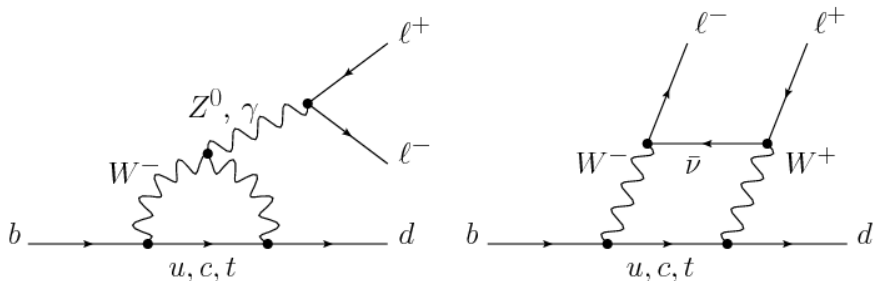


Figure 1.5: Loop Feynmann diagrams allowing $b \rightarrow d$ FCNC processes: penguin diagram (left) and W box (right).

²⁴⁷ 1.5.1 Theoretical framework: the effective Hamiltonian

²⁴⁸ Rare decays of b hadrons are governed by an interplay between weak and strong
²⁴⁹ interactions. The large masses of W , Z and top quark compared to that of the b quark
²⁵⁰ allow the construction of an effective theory that divides the problem of calculating
²⁵¹ weak decay amplitudes into two parts: “short-distance” and “long-distance” effects
²⁵² separated at an energy scale μ . The first part, dealing with short distance physics,
²⁵³ handles perturbative contributions due to energy scales above the b mass. The
²⁵⁴ second part typically deals with non-perturbative contributions. A classic example
²⁵⁵ of an effective theory is the Fermi theory of weak interactions which describes the
²⁵⁶ β decay in terms of a four-fermion interaction, where the short distance physics is
hidden into a point like vertex as illustrated in Fig. 1.6.

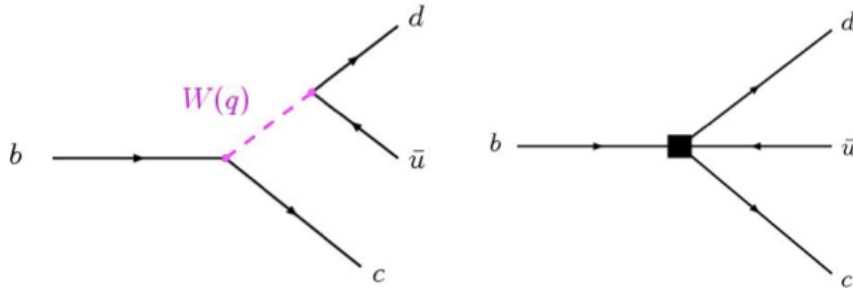


Figure 1.6: Example of a Fermi theory in which the full theory is divided between a short distance contribution, hidden in the vertex, and a long distance contribution.

²⁵⁷

²⁵⁸ The effective hamiltonian [24] relevant to $b \rightarrow s/d\gamma$ and $b \rightarrow s/d\ell^+\ell^-$ transitions
²⁵⁹ can be written as:

$$\mathcal{H}_{eff} = \frac{-4G_F}{\sqrt{2}} \left[\lambda_q^t \sum C_i(\mu, M) \mathcal{O}_i(\mu) + \lambda_q^u \sum C_i(\mu, M) (\mathcal{O}_i(\mu) - \mathcal{O}_i^u(\mu)) \right], \quad (1.6)$$

²⁶⁰ where G_F denotes the Fermi coupling constant and the λ constants are the CKM
²⁶¹ factors, $\lambda_q^t = V_{tb}V_{tq}^*$ and $\lambda_q^u = V_{ub}V_{uq}^*$. In $b \rightarrow s$ quark transitions, which are the
²⁶² main topic of this thesis, the doubly Cabibbo-suppressed contributions proportional
²⁶³ to λ_s^u can be neglected. To obtain this formula the Operator Product Expansion
²⁶⁴ (OPE) [25] method is used, which implements a summation over all contributing
²⁶⁵ operators weighted by corresponding constants called Wilson coefficients. In this

266 Hamiltonian the long-distance contributions are described by the operators, \mathcal{O}_i ,
267 while the short-distance physics is encoded in the Wilson Coefficients, C_i . Operators
268 and coefficients are evaluated at the renormalization scale μ . Any particle that
269 contributes to the decay and has a mass greater than the scale μ will affect the
270 value of at least one of the Wilson coefficients, including SM particles as the top
271 quark.

272 In order to describe SM processes the effective theory must be matched with the
273 SM by requiring the equality between each term in effective theory and the full
274 theoretical calculation at a matching scale, typically the EW scale (μ_W). Then, using
275 the scale independence of the effective Hamiltonian, one can derive a renormalization
276 group equation for the Wilson Coefficients

$$\mu \frac{d}{d\mu} C_i(\mu) = \gamma_{ij} C_j(\mu), \quad (1.7)$$

277 where the matrix γ is the anomalous dimensions matrix of the operators \mathcal{O}_i . At
278 leading order the solution is given by [26]:

$$C_i(\mu) = \left[\frac{\alpha_s(\mu_W)}{\alpha_s(\mu)} \right]^{\frac{\gamma_{ii}^0}{2\beta_0}} C_i(\mu_W) = \left[\frac{1}{1 + \beta_0 \frac{\alpha_s(\mu)}{4\pi} \ln \frac{\mu_W^2}{\mu^2}} \right]^{\frac{\gamma_{ii}^0}{2\beta_0}} C_i(\mu_W), \quad (1.8)$$

279 where α_s is the strong coupling constant. In the SM, using $\mu_W = m_b$, the Wilson
280 Coefficients have values:

$$C_7^{SM} = -0.3, \quad C_9^{SM} = 4.2, \quad C_{10}^{SM} = -4.2 \quad (1.9)$$

281 and new physics contributions appear in the Wilson Coefficients in the form of
282 additive factors:

$$C_i = C_i^{NP} + C_i^{SM}. \quad (1.10)$$

283 The amplitudes of exclusive hadronic decays can be calculated as the expectation
284 values of the effective Hamiltonian. Given an initial state I and a final state F

²⁸⁵ (e.g. $I = B$ and $F = K^{*0}\mu^+\mu^-$) the decay amplitude can be calculated as

$$A(I \rightarrow F) = \langle I | \mathcal{H}_{eff} | F \rangle == \frac{G_F}{\sqrt{2}} \sum V_{CKM}^i C_i(\mu) \langle I | \mathcal{O}_i(\mu) | F \rangle, \quad (1.11)$$

²⁸⁶ where $\langle I | \mathcal{O}_i(\mu) | F \rangle$ are the hadronic matrix elements also called “form factors”.

²⁸⁷ These can be evaluated using non perturbative methods such as lattice calculations.

²⁸⁸ However, due to the limitations of these methods, they represent the dominant

²⁸⁹ source of uncertainty in theoretical calculations.

²⁹⁰ 1.5.2 Operators

²⁹¹ Separating the left- and right-handed components the effective Hamiltonian is

$$\mathcal{H}_{eff} = \frac{4G_F}{\sqrt{2}} V_{tb} V_{ts}^* \frac{\alpha_e}{4\pi} \sum_{i=1}^{10} [C_i \mathcal{O}_i + C'_i \mathcal{O}'_i]. \quad (1.12)$$

²⁹² A complete basis is given by a set of 10 operators, where $\mathcal{O}_{1,2}$ are the tree level

²⁹³ W operators; $\mathcal{O}_{3-6,8}$ are penguin diagrams mediated by gluons; and $\mathcal{O}_{7,9,10}$, which

²⁹⁴ are the operators that are relevant for radiative and leptonic penguin processes are

²⁹⁵ defined as [21]:

$$\begin{aligned} \mathcal{O}_7 &= \frac{m_b}{e} (\bar{s}\sigma^{\mu\nu}P_R b)F_{\mu\nu}, & \mathcal{O}'_7 &= \frac{m_b}{e} (\bar{s}\sigma^{\mu\nu}P_L b)F_{\mu\nu}, \\ \mathcal{O}_9 &= (\bar{s}\gamma_\mu P_L b)(\bar{\ell}\gamma^\mu \ell), & \mathcal{O}'_9 &= (\bar{s}\gamma_\mu P_R b)(\bar{\ell}\gamma^\mu \ell), \\ \mathcal{O}_{10} &= (\bar{s}\gamma_\mu P_L b)(\bar{\ell}\gamma^\mu \gamma_5 \ell), & \mathcal{O}'_{10} &= (\bar{s}\gamma_\mu P_R b)(\bar{\ell}\gamma^\mu \gamma_5 \ell), \end{aligned} \quad (1.13)$$

²⁹⁶ where $P_{L/R} = (1 \mp \gamma_5)/2$ denote the left/right handed chiral projection, T^a are the

²⁹⁷ QCD generators and $F_{\mu\nu}$ is the electromagnetic field tensor. The \mathcal{O}' operators cor-

²⁹⁸ respond to right-handed coupling obtained by swapping P_R and P_L in the equations.

²⁹⁹ In the SM, as well as in MFV models where the flavour violation is entirely ruled by

³⁰⁰ the CKM matrix, the C' Wilson Coefficients are suppressed by the strange coupling,

³⁰¹ $C'_i \sim (m_s/m_b)C_i$. The operator \mathcal{O}_7 relates to penguin diagrams that are mediated

³⁰² via a photon. It represents the dominant contribution to the radiative $b \rightarrow s\gamma$

303 transition and contributes to $b \rightarrow s\ell^+\ell^-$ processes when the virtual photon decays
304 into a dilepton pair. The semileptonic \mathcal{O}_9 and \mathcal{O}_{10} correspond to penguin diagrams
305 mediated by a Z boson and W mediated box diagrams. These are the dominant
306 contributions in semileptonic $b \rightarrow s\ell^+\ell^-$ decays. The vertices corresponding to the
radiative and semileptonic operators are illustrated in Fig. 1.7

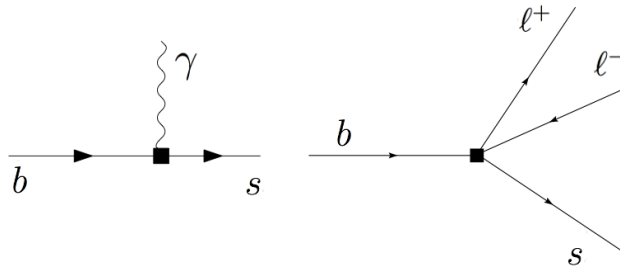


Figure 1.7: Interaction vertices corresponding to the radiative (left) and semileptonic (right) operators.

307

308 It is also common to express the semileptonic operators in a basis with left and right
309 projected leptons

$$\begin{aligned} \mathcal{O}_{LL} &= (\mathcal{O}_9 - \mathcal{O}_{10})/2 & \mathcal{O}_{LR} &= (\mathcal{O}_9 + \mathcal{O}_{10})/2 \\ \mathcal{O}_{RR} &= (\mathcal{O}'_9 - \mathcal{O}'_{10})/2 & \mathcal{O}'_{RL} &= (\mathcal{O}'_9 + \mathcal{O}'_{10})/2 \end{aligned} \quad (1.14)$$

310 where the Wilson Coefficients are redefined as

$$\begin{aligned} C_{LL} &= C_9 - C_{10}, & C_{LR} &= C_9 + C_{10}, \\ C_{RR} &= C'_9 - C'_{10}, & C'_{RL} &= C'_9 + C_{10}. \end{aligned} \quad (1.15)$$

311 This basis is particularly useful in frameworks where BSM physics at a high mass
312 scale respects the $SU(2)_W$ part of the SM gauge symmetry group. Finally, in the
313 picture presented in this section all operators were considered as universal with
314 respect of the flavour of the involved leptons. However, BSM models often contain
315 sources of lepton universality violation leading to a split of the same operators
316 depending on the lepton considered: $C_i \rightarrow C_i^e, C_i^\mu, C_i^\tau$ and $\mathcal{O}_i \rightarrow \mathcal{O}_i^e, \mathcal{O}_i^\mu, \mathcal{O}_i^\tau$.

317 1.5.3 Phenomenology of $b \rightarrow s\ell^+\ell^-$ decays

318 Semileptonic b hadron decays are characterised by two kinematic regimes which are
 319 treated theoretically in different ways; Table 1.3 shows a scheme of the q^2 spectrum.
 320 The ‘high q^2 ’ is the region of low hadron recoil, $q^2 > 15 \text{ GeV}^2/c^4$, and is charac-
 321 terised by the energy of the hadron being less than the energy scale of QCD interac-
 322 tions within the meson, $\Lambda_{QCD} \sim 1 \text{ GeV}$. In this region theoretical calculations of B
 323 meson decays can be simplified by working in the heavy quark limit, $m_b \rightarrow \infty$. In
 324 this limit a Heavy Quark Effective Theory (HQET) [27] can be constructed in which
 325 the heavy quark interacts only via ‘soft’ hadronic processes and an OPE in $1/m_b$ is
 326 valid. The ‘low q^2 ’ is instead the region where the light spectator quark is energetic
 327 and cannot be neglected. Furthermore, the light quark interacts not only via ‘soft’
 328 hadronic processes, as in HQET, but also via the so-called ‘collinear’ hadronic pro-
 329 cesses. The boundary of this region can be set at $\sim 7 \text{ GeV}^2/c^4$ which corresponds
 330 to the threshold for $c\bar{c}$ production, $(2m_c)^2$. In this region the hadronic interactions
 331 are handled by expanding in terms of the energy of the emitted energetic hadron,
 332 $1/E_h$, forming the so-called Soft-Collinear Effective Theory (SCET) [28]. In both
 333 regions decay rates can be predicted using the different methods and the biggest un-
 334 certainties come from the limited knowledge of hadronic transition matrix elements.
 335 The intermediate region is characterised by the presence of charmonium resonances,
 336 produced through tree level $b \rightarrow c\bar{c}s$ transitions and no precise theoretical calculation
 337 is available [29].

338 As can be seen in Fig. 1.8 the very low q^2 is characterised by a peak due to the
 339 virtual photon contribution, associated with C_7 . In the region $1 - 6 \text{ GeV}^2/c^4$ the
 340 interference between C_7 and C_9 becomes large, yielding sensitivity to NP in C_9 .
 341 The $7 - 15 \text{ GeV}^2/c^4$ interval is dominated by the charmonium resonances, J/ψ and
 342 $\psi(2S)$. Although these decays can be experimentally vetoed in principle charmonia

Table 1.3: A scheme of the q^2 spectrum.

$q^2 = 0$	$E_{K^{*0}} >> \Lambda_{QCD}$	$q^2 \sim m_{J/\psi, \psi(2S)}^2$	$E_{K^{*0}} \sim \Lambda_{QCD}$	$q^2 = (m_B - m_K^{*0})^2$
max. recoil	large recoil (SCET)	$c\bar{c}$ resonances	low recoil (HQET)	zero recoil

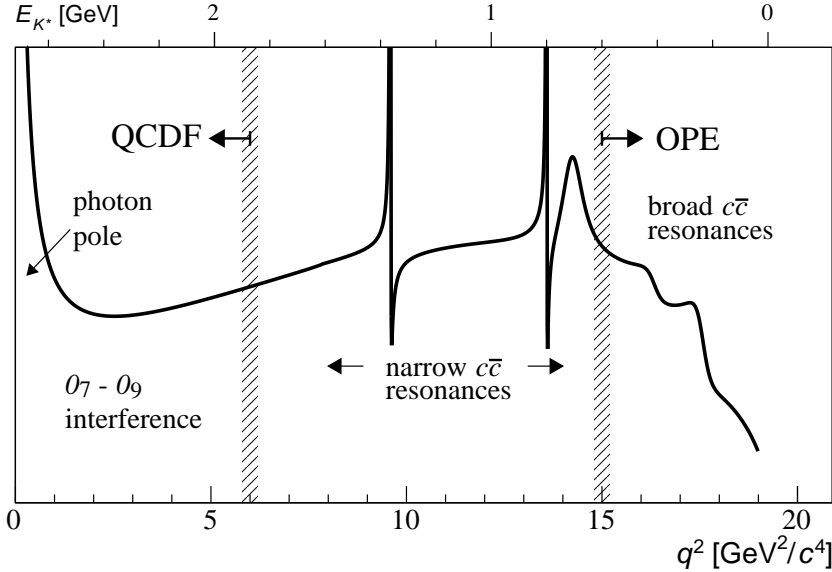


Figure 1.8: A typical q^2 spectrum of $b \rightarrow s\ell^+\ell^-$ process characterised by the photon pole at very low q^2 , charmonium resonances at central q^2 and broad resonances at high q^2 .

³⁴³ affect the entire q^2 space. Finally, at high q^2 broad charmonium resonances can
³⁴⁴ contribute, like those observed by LHCb in $B^+ \rightarrow K^+\mu^+\mu^-$ decays [30].

³⁴⁵ 1.5.4 Observables in $b \rightarrow s\ell^+\ell^-$ decays

³⁴⁶ Rare decays and especially semileptonic $b \rightarrow s\ell^+\ell^-$ processes offer a number of ob-
³⁴⁷ servables which can be used to benchmark BSM models. The most direct effects
³⁴⁸ appear in decay rates that can be enhanced by new physics but the precision on
³⁴⁹ these measurements is often limited by the uncertainty on form factor calculations.
³⁵⁰ Therefore, it is important to also look for different observables. One important
³⁵¹ class of observables are angular quantities that can often carry complementary in-
³⁵² formation with respect to branching ratio measurements. The most basic of these
³⁵³ observable are forward-backward asymmetries that characterise the angular distri-
³⁵⁴ bution of final particles. For the $B^0 \rightarrow K^*\mu^+\mu^-$ decay combinations of observables
³⁵⁵ have been proposed that are independent of form factor uncertainties at leading
³⁵⁶ order order [21].

357 An other way to build safe observables is to construct ratios between similar decays,
 358 in which uncertainties due to the hadronization process cancel out. These observ-
 359 ables include the R_H ratios, between B^0 decays into electrons and muons, that are
 360 described in detail in Ch. ???. It is also interesting to compare decays which go
 361 though the same fundamental process but where the spectator quark has a different
 362 flavour. This is the case of $B^+ \rightarrow K^+ \mu^+ \mu^-$ and $B^0 \rightarrow K_s^0 \mu^+ \mu^-$ decays, which are
 363 both $b \rightarrow s$ transitions where the spectator quark is an u quark in the first case
 364 and a d quark in the second. The ratio of the branching fractions of these decays is
 365 called isospin asymmetry.

366 1.6 Experimental status

367 To set the background for the analysis described in this thesis, this section reports a
 368 brief review of recent results of new physics searches involving rare decays or lepton
 369 flavour violation. Among these, results recently obtained by the LHCb experiment
 370 show a series of anomalies with respect to the SM that have the potential to yield
 371 to BSM scenarios.

372 1.6.1 Dimuon decays of b hadrons

Decays of B mesons into a dimuon are two-body decays where the two muons are back to back in the hadron rest frame. The simple signatures of these decays makes them easy to study and the fact that they are unaffected by hadronic physics in the final state makes predictions very clean and precise. Therefore these are essential tests of the SM. The $B^0 \rightarrow \mu^+ \mu^-$ and $B_s^0 \rightarrow \mu^+ \mu^-$ decays are exceedingly rare in the SM. First of all they are FCNCs that can only happen in loops and furthermore they are CKM-suppressed. In addition to that the decay of a pseudo-scalar B meson into two muons has a significant helicity suppression. The latest SM predictions for

these decay rates are [31]:

$$\mathcal{B}(B_s^0 \rightarrow \mu^+ \mu^-) = (3.65 \pm 0.23) \times 10^{-9} \text{ and} \quad (1.16)$$

$$\mathcal{B}(B^0 \rightarrow \mu^+ \mu^-) = (1.06 \pm 0.09) \times 10^{-10}. \quad (1.17)$$

The uncertainties on these values mainly come from the knowledge of the decay constants and CKM-elements. BSM models can produce significant enhancement to these decay rates. Furthermore, the measurement of their ratio is a stringent test of the MFV hypothesis. A combination of the LHCb and CMS results measured the values [32]:

$$\mathcal{B}(B_s^0 \rightarrow \mu^+ \mu^-) = (2.8^{+0.7}_{-0.6}) \times 10^{-9} \text{ and} \quad (1.18)$$

$$\mathcal{B}(B^0 \rightarrow \mu^+ \mu^-) = (3.9^{+1.6}_{-1.4}) \times 10^{-10}. \quad (1.19)$$

373 Both decays were previously unobserved, while now the B_s^0 decay is observed with
374 a significance of 6σ and evidence for the B^0 decay is found at 3σ significance level.
375 The measured branching fractions are compatible with SM predictions within 2σ and
376 put strong constraints to the available parameter-space for BSM theories. Figure 1.9
377 shows the fit the dimuon invariant mass of B meson candidates where the peaks of
378 the two decays are visible.

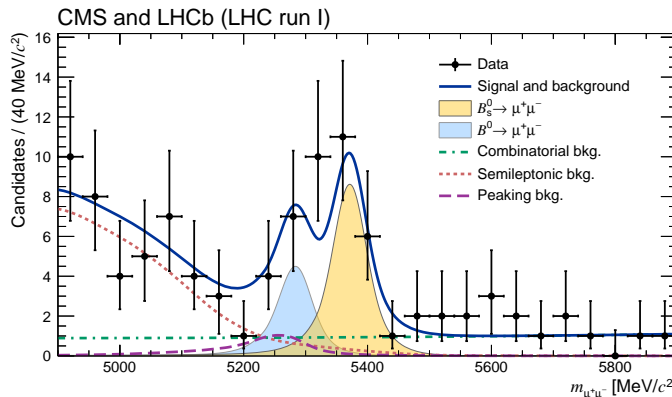


Figure 1.9: Dimuon invariant mass of B candidates showing peaks corresponding $B_s^0 \rightarrow \mu^+ \mu^-$ and $B^0 \rightarrow \mu^+ \mu^-$ decays [32].

³⁷⁹ **1.6.2 Semileptonic $b \rightarrow s\ell^+\ell^-$ decays of b hadrons**

³⁸⁰ At the LHC energies is now possible to collect large data samples of semileptonic
³⁸¹ decays, especially those with muons in the final state. Many branching fractions
³⁸² of semileptonic B meson decays were recently measured at the LHCb experiment,
³⁸³ including $B \rightarrow K\mu^+\mu^-$, $B \rightarrow K^{*0}\mu^+\mu^-$ and $B_s^0 \rightarrow \phi\mu^+\mu^-$ [33, 34, 35]. Baryon
³⁸⁴ decays were also studied at LHCb: including the rare $\Lambda_b \rightarrow \Lambda\mu^+\mu^-$ decay [36], whose
³⁸⁵ analysis is described in this thesis. Unlike for pure leptonic decays, SM predictions
³⁸⁶ for semileptonic decays are affected by the knowledge of hadronic form factors, which
³⁸⁷ results in relatively large uncertainties, $\mathcal{O}(30\%)$. As a result measurements are now
³⁸⁸ typically more precise than predictions.

³⁸⁹ Among the measurements of angular observables that can be affected by new physics,
³⁹⁰ particular interest was risen by the measurement of a set of observables in $B \rightarrow$
³⁹¹ $K^{*0}\mu^+\mu^-$ decays, free from form factors uncertainties at leading order [37]. Most of
³⁹² the measurements are found to be in agreement with SM predictions with the excep-
³⁹³ tion of the P'_5 observable, shown in Fig. 1.10, which presents a local 3.7σ deviation.
³⁹⁴ Attempts to build a consistent picture point to a new physics contribution to the
³⁹⁵ Wilson Coefficient C_9 [38]. An angular analysis of $B^+ \rightarrow K^+\mu^+\mu^-$ decays was also
³⁹⁶ performed, where observables are found to be compatible with SM predictions [39].

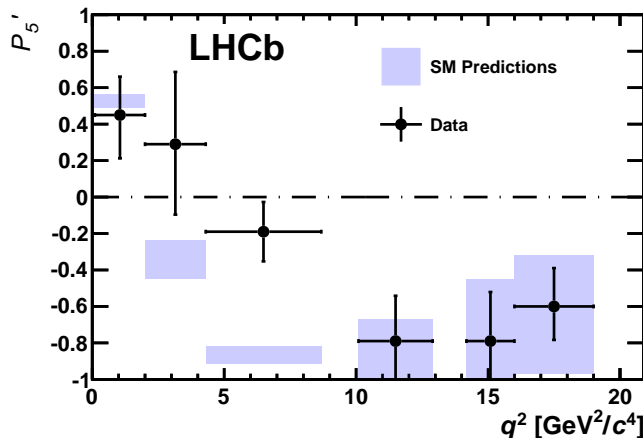


Figure 1.10: Measurement of the observable as a function of q^2 , showing a tension with SM predictions in the 2–6 GeV^2/c^4 region.

q^2 [GeV $^2/c^4$]	$B^0 \rightarrow K^+ \mu^+ \mu^-$		$B^0 \rightarrow K^{*0} \mu^+ \mu^-$	
	1.1–6	15.0–22.0	1.1–6	15.0–19.0
\mathcal{A}_{CP}	0.004 ± 0.028	-0.005 ± 0.030	0.094 ± 0.047	-0.074 ± 0.044
\mathcal{A}_I	$-0.10^{+0.08}_{-0.09} \pm 0.02$	$-0.09 \pm 0.08 \pm 0.02$	$0.00^{+0.12}_{-0.10} \pm 0.02$	$0.06^{+0.10}_{-0.09} \pm 0.02$

Table 1.4: Measurement of CP and isospin asymmetry in $B^0 \rightarrow K^{(*)} \mu^+ \mu^-$ decays from the LHCb experiment.

398 Other observables for which the sensitivity to form factors effects is reduced are the
 399 CP asymmetry between B and \bar{B} decays, \mathcal{A}_{CP} , and the isospin asymmetry between
 400 B^0 ad B^+ decays, \mathcal{A}_I . Due to the small size of the corresponding CKM elements
 401 CP asymmetries of $B^0 \rightarrow K^{(*)} \mu^+ \mu^-$ decays are tiny in the SM, $O(10^{-3})$. In BSM
 402 models new sources of CP violation can arise and therefore \mathcal{A}_{CP} measurements are
 403 a powerful null test of the SM. The isospin asymmetry is not zero in the SM due
 404 to isospin breaking effects in the form factors. This is expected to be $\sim 1\%$ at low
 405 q^2 and increase to $\sim 10\%$ as q^2 tends to zero. The LHCb experiment, using the
 406 full dataset collected in Run I, corresponding to an integrated luminosity of 3 fb^{-1} ,
 407 measured both these asymmetries to be consistent with zero [33, 40], as reported in
 408 Tab. 1.4.

409 Recently, progress was made measuring also electron channels. The branching frac-
 410 tion of the $B^0 \rightarrow K^{*0} e^+ e^-$ decay was measured to be $(3.1 \pm 1.3) \times 10^{-7}$ in the
 411 dilepton mass interval 30 – $1000 \text{ MeV}/c^2$ [41]. Furthermore, for the first time angu-
 412 lar observables were measured for this decay and found to be consistent with SM
 413 predictions [42].

414 1.6.3 Lepton Flavour Violation searches

415 Several Lepton Flavour Violation (LFV) searches are linked to rare decays as they
 416 involve small branching ratios in the SM that can be enhanced by new physics. They
 417 are therefore a natural place to look for new physics. Lepton flavour conservation is
 418 well experimentally established measuring the branching ratios of decays of muons
 419 into electrons and no neutrinos but has no strong theoretical explanation in the

⁴²⁰ context of the SM. In fact it is already observed that flavour is not conserved in
⁴²¹ neutrino oscillations.

⁴²² The best-studied decays violating lepton flavour are rare muon decays including
⁴²³ $\mu^+ \rightarrow e^+\gamma$ and $\mu^+ \rightarrow e^+e^-e^+$. Since muons can be abundantly produced and
⁴²⁴ the final states are simple, these decays provide the best constraints to LFV. The
⁴²⁵ present best upper limits are 1.2×10^{-11} for the radiative decay and 1.0×10^{-12}
⁴²⁶ for $\mu^+ \rightarrow e^+e^-e^+$ obtained respectively by the MEGA [43] and SINDRUM [44] ex-
⁴²⁷ periments. Several LFV searches in the B sector have recently been performed at
⁴²⁸ the LHCb experiment including decays such as $B^0 \rightarrow e\mu$ [45] and τ decays such as
⁴²⁹ $\tau \rightarrow \mu^+\mu^-\mu^-$ [46]. None of these searches has found evidence of new physics so far
⁴³⁰ and therefore they set limits, constraining the parameter space available for BSM
⁴³¹ models. Figure 1.11 shows a summary of the best limits set at different times on
⁴³² LFV searches [47].

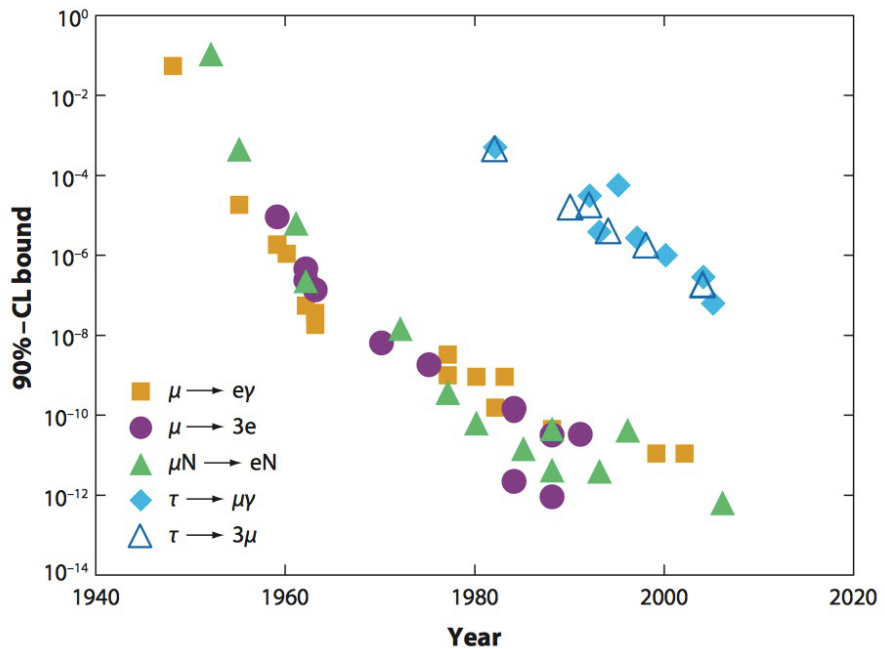


Figure 1.11: Summary of limits set in LFV searches as a function of time [47].

433

CHAPTER 2

434

435

The LHCb detector at the Large Hadron Collider

436

437

2.1 The Large Hadron Collider

438 The Large Hadron Collider (LHC) [48] is a circular particle accelerator with a cir-
439 cumference of 27 km located about 100 m underground at CERN in the surroundings
440 of Geneva, Switzerland. Two proton beams circulate in opposite directions around
441 the ring and cross each other in four points, in which particle detectors are placed.
442 These include two general-purpose detectors, ATLAS and CMS, sitting on opposites
443 sides of the ring and two smaller detectors, ALICE and LHCb that are designed to
444 study specific topics (see Fig. 2.1).

445 Each beam consists of a series of proton bunches, up to a maximum of 2835. Each
446 bunch consists of about 10^{11} protons and the bunch spacing is such that the nom-
447 inal bunch crossing rate is 40 MHz. The beams are injected into pre-accelerators
448 and then led into LHC through the CERN acceleration system shown in Fig. 2.1.

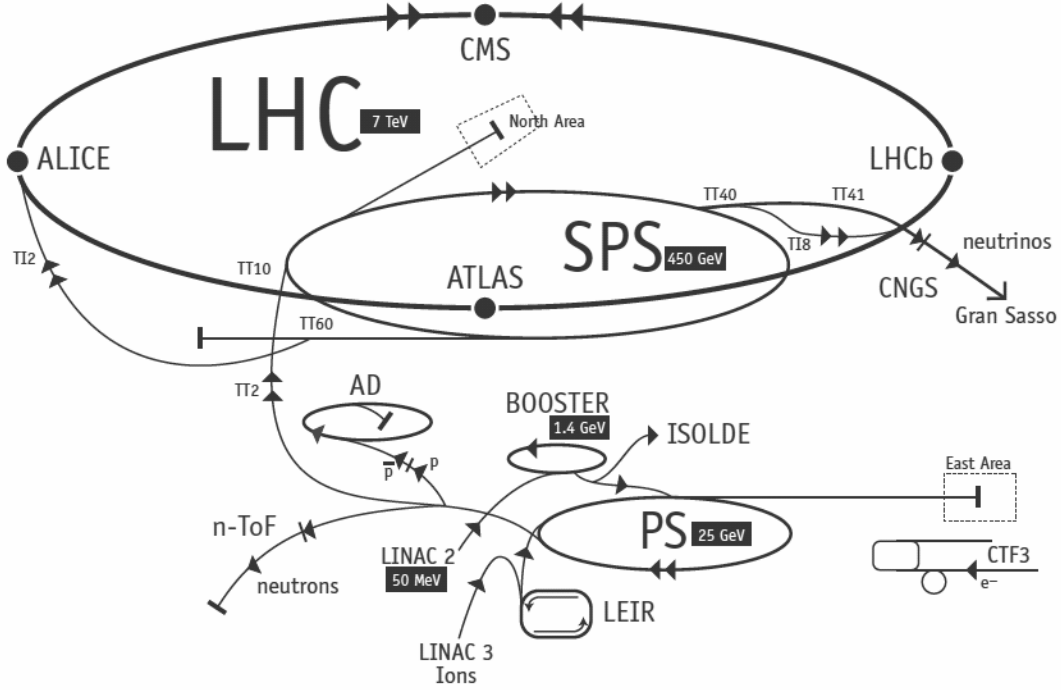


Figure 2.1: Scheme of CERN accelerators.

449 Protons are produced from hydrogen gas and are initially accelerated to the energy
 450 of 50 MeV in a linear accelerator (LINAC). Then they are injected into the Proton
 451 Synchrotron Booster (PSB), where they are boosted to an energy of 1.4 GeV, into
 452 the Proton Synchrotron (PS) to 25 GeV and into the Super Proton Synchrotron
 453 (SPS) to 450 GeV. Finally, protons enter into the LHC storage ring, where they are
 454 accelerated from injection energy to the final one by radio frequency (RF) cavities.
 455 The beams are steered around the ring by 8 T magnetic fields produced by 15 m
 456 long superconducting niobium-titanium dipole magnets and focused by quadrupole
 457 magnets. The LHC magnets use a design in which both proton beam pipes are
 458 contained in the same housing, allowing the same liquid helium to cool the system
 459 down for both. The LHC began colliding proton beams in physics mode in 2009 at
 460 a center of mass energy of $\sqrt{s} = 900$ GeV and from April 2010 to November 2011
 461 accelerated beams at $\sqrt{s} = 7$ TeV (3.5 TeV per proton beam) with a maximum
 462 instantaneous luminosity of $3 \cdot 10^{33} \text{ cm}^{-2}\text{s}^{-1}$, while in 2012 the energy was increased
 463 to 8 TeV. The LHC maximum design energy is 14 TeV, and its design luminosity is
 464 $10^{34} \text{ cm}^{-2}\text{s}^{-1}$. After a long shut down to upgrade and maintain the machine, a new

465 run started in June 2015, in which protons are collided at a center of mass energy
466 of $\sqrt{s} = 13$ TeV. At this energy the total proton-proton cross section is expected to
467 be roughly 100 mb.

468 **2.2 The LHCb detector**

469 The LHCb detector [49] was built to study decays of B and D mesons, mainly
470 looking for CP-violating processes. In 2011, running at a centre of mass energy of
471 7 TeV, the cross section for $b\bar{b}$ production was measured to be $284 \pm 53 \mu b$ [50],
472 while it will be $\sim 500 \mu b$ at the current LHC energy, 13 TeV. At these high energies,
473 proton-proton interactions produce highly boosted virtual gluons which produce $b\bar{b}$
474 pairs at small angles, close to the beam pipe. For this reason the LHCb detector is
475 designed to have a very forward angular coverage. The detector is fully instrumented
476 from 10 mrad to 300 mrad, corresponding to an interval $2 < \eta < 5$, where η is the
477 “pseudorapidity”, a quantity used in particle physics defined as:

$$\eta = -\ln(\tan(\theta/2)), \quad (2.1)$$

478 where θ is the angle between a particle’s momentum and the beam direction ¹.

479 At LHCb’s collision point the luminosity can be adjusted by displacing the beams
480 from head on collisions while keeping the same crossing angle allowing the experi-
481 ment to keep an approximately constant instantaneous luminosity. This means that
482 the average number of interactions per bunch crossing can be limited, which is im-
483 prtant because the detector efficiency, especially in detecting secondary vertices,
484 decreases for events with an high number of primary vertices (PV). Reducing the
485 particle occupancy through the detector also keeps radiation damage to a minimum.
486 Since the LHC started colliding protons in November 2009 until the end of 2011,

¹LHCb’s reference system has the z axis in the direction of the beam, the x axis directed to the centre of the accelerator and y is directed upward. Then we define θ as the angle with the beam direction and ϕ as the position around the beam in the xy plane, taking $\phi = 0$ on the x axis. The origin, $(x, y, z) = (0, 0, 0)$, corresponds to the center of the interaction area.

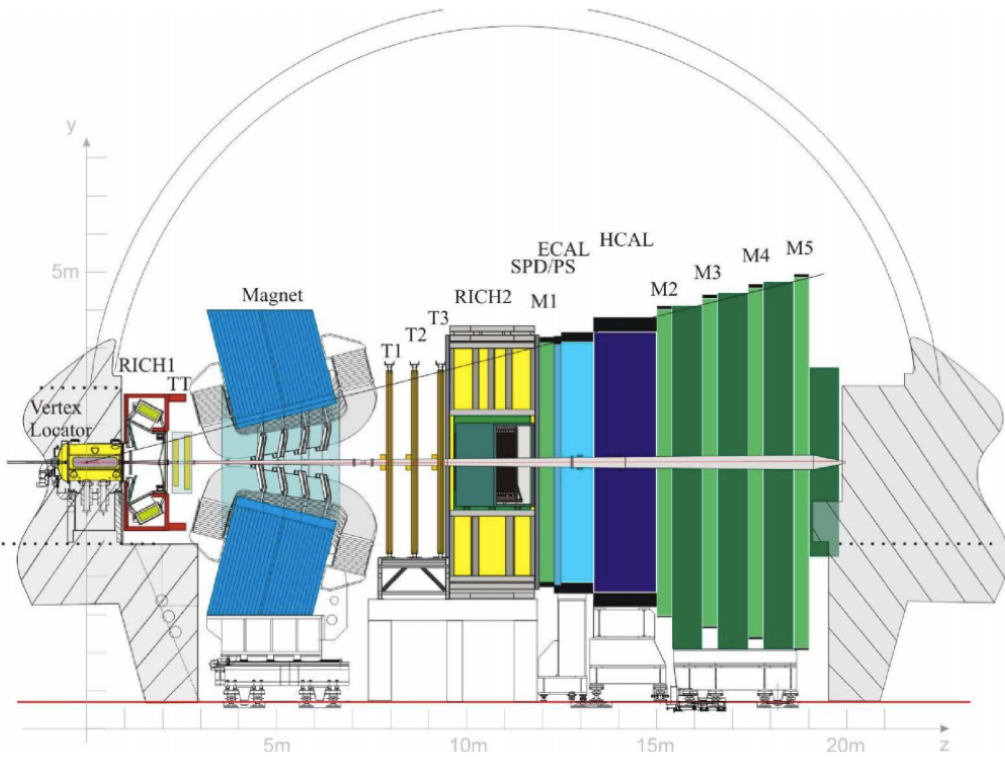


Figure 2.2: A side view of the LHCb detector [49].

487 the instantaneous luminosity was at an average of $3 \cdot 10^{32} \text{ cm}^{-2}\text{s}^{-1}$, corresponding
 488 to an average number of 1.5 PVs per bunch crossing. At the end of 2011 LHCb had
 489 collected an integrated luminosity of 1 fb^{-1} ; in 2012 the luminosity was increased
 490 and 2 fb^{-1} more were collected.

491 Other B physics experiments, like BaBar at the Stanford Linear Accelerator (SLAC),
 492 Belle at KEK at J-PARC (Japan) and the Tevatron experiments at Fermilab have
 493 made accurate measurements in heavy flavour physics. All of these results have
 494 so far been consistent with the Standard Model predictions. However, some of the
 495 deviations from the Standard Model are expected to be very small. Therefore LHCb
 496 was designed to make the most precise measurements in heavy flavour physics to
 497 test the consistency of the Standard Model and look for new physics.

498 The LHCb detector includes a high-precision tracking system consisting of a silicon-
 499 strip vertex detector surrounding the pp interaction region, and a larger silicon-strip
 500 and drift tubes detectors located on both sides of a dipole magnet with a bend-

ing power of about 4 Tm. Charged hadrons are identified using two Ring-Imaging Cherenkov detectors (RICH) [51]. Photon, electron and hadron candidates are identified by a calorimeter system and muons by a system composed of alternating layers of iron and multi-wire proportional chambers [52]. A schematic view of the detector is shown in Fig. 2.2 and more details on each sub-detector are given in the following sections.

2.3 The magnet

Charged particle are bent horizontally in the magnetic field so that their momentum can be measured from the curvature radius. The LHCb dipole magnet is composed of two coils supported by an iron yoke and is shaped to fit the LHCb angular acceptance. Unlike the other LHC experiments, LHCb uses a warm magnet, so that it can be easily ramped which allows to reverse the field periodically. As when the polarity is flipped particles of a given sign are bent in the opposite direction, this method is used to limit systematic uncertainties that can arise from different performances in different areas of the detector and average out using data taken in both polarities. In the magnet flows a 5.85 kA current that generates an integrated magnetic field of 4 Tm for 10 m long tracks. In order to achieve the required momentum precision the magnetic field must be mapped with a 10^{-4} precision. For this reason a grid of 60 sensors is positioned inside the magnet and provides real time magnetic field maps.

2.4 Tracking system

B mesons have lifetimes of approximately 1.5 ps. At the LHC energies, this means they travel about 1 cm before decaying forming a displaced vertex. To study specific decays, it is therefore important to be able to separate the particles produced at the primary pp vertex and at the B decay secondary vertex (SV). The tracking

system consists in the Vertex Locator (VeLo), and 4 tracking stations: the Tracker Turicensis (TT), which are located before the magnet and the T1, T2 and T3 stations, located after of the magnet. The latter tree stations are in turn formed by two subsystems: the Inner Tracker (IT) close to the beam-line, where the particle density is greatest, and the Outer Tracker (OT) covering the rest of the acceptance.

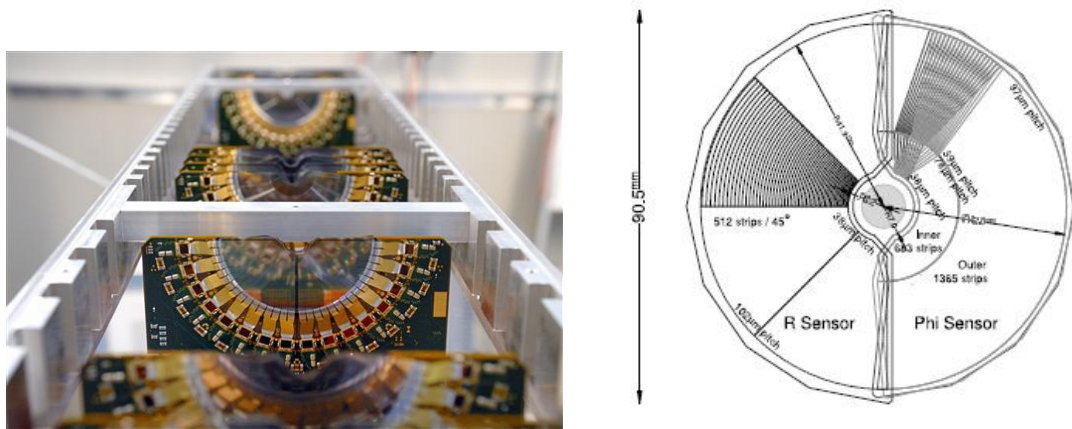


Figure 2.3: On the left VeLo sensors mounted in line and on the right a schematic view of one sensor [49].

531

The VeLo accurately measures positions of tracks close to the interaction point which is essential to reconstruct production and decay vertices of bottom and charm hadrons. The VeLo is composed by 21 silicon modules which surround the beam axis and are positioned from $z = -18$ cm to $+80$ cm. The sensitive region of the VeLo starts at an inner diameter of only 8 mm from the beam axis and it is able to detect particles within a pseudorapidity range $1.6 < \eta < 4.9$. The VeLo is housed in its own vacuum vessel of thin aluminium foil, which protects the vacuum of the beam pipe from any outgassing. The silicon layers composing the VeLo consist of two modules each including two types of sensors: the ϕ -sensor, which measures the azimuthal position around the beam, and the R-sensor, which measures the radial distance from the beam axis. A sketch of the VeLo sensors is shown in Fig. 2.3. The sensors are $300 \mu\text{m}$ thick and to ensure that they cover the full azimuthal angle the right-side module is placed 1.5 cm behind the left-side module on the z-axis and

545 they overlap. There are two modules which cover the backward direction and are
546 used as a veto for multiple interactions, this is called the pileup system.

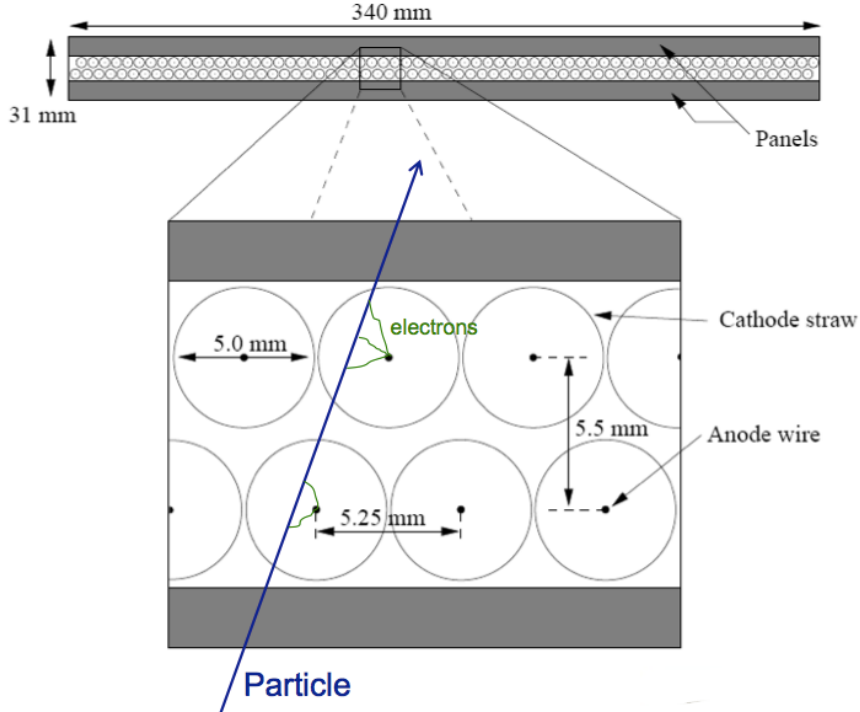


Figure 2.4: Sketch of the straw tubes which constitute the Outer Tracker layers [49].

547

548 The IT and TT both use silicon strips and together constitute the Silicon Tracker
549 (ST). Straw tubes are instead used in the OT, of which a sketch is shown in Fig. 2.4.
550 The IT requires an higher inner granularity because of the higher flux of particles
551 close to the beam pipe. In fact it covers only 1.3% of the total area of IT plus
552 OT but it contains about 20% of the tracks. Each ST station has four detection
553 layers: the first and last are vertical, measuring the track position in x , while the
554 second and third layers are rotated by an angle of +5 and -5 degrees, which allows
555 to measure the y coordinate. The TT is placed upstream of the magnet to allow
556 the reconstruction of tracks from low-momentum particles, which are bent out of
557 the downstream acceptance. Overall the tracking system provides a measurement of
558 momentum, p , with a relative uncertainty that varies from 0.4% at 5 GeV/ c to 1.0%
559 at 200 GeV/ c . The impact parameter (IP), namely the minimum distance of a track

to a primary vertex, is measured with a resolution of $(15 + 29/p_T) \mu m$, where p_T is the component of the momentum transverse to the beam, in GeV/c . The z -axis position of a PV reconstructed with 35–40 tracks can be measured with a precision of roughly $50\text{--}60 \mu m$. Accurate IP and vertex displacement measurements allow LHCb to effectively distinguish between B meson decays and background processes. In fact B mesons typically travel $\sim 1 \text{ cm}$ in the detector before decaying into lighter particles, which tend to have high IP as the B decay imparts transverse momentum to them.

2.5 Calorimeters

The main purpose of the calorimeter system is to determine the energy of particles but in LHCb it is also extensively used to identify electron and hadrons. In general a calorimeter is composed by layers of absorber and active material. Particles interact with the absorber layers and produce a cascade of secondaries, which multiply quickly and are detected by the active part usually composed of scintillating layers. The light produced is detected by photo-multipliers (PMTs) and it is approximately proportional to the energy of the deposited particles. Calibration is then used to translate the signal into an energy measurement. The LHCb’s calorimeter system consists of the Scintillator Pad Detector (SPD), the Pre-Shower Detector (PS) as well as the Electromagnetic Calorimeter (ECAL) and the Hadronic Calorimeter (HCAL). A sketch of the LHCb calorimeters is shown in Fig. 2.5. The SPD/PS cells are read out with PMTs located outside the LHCb acceptance, while the ECAL and HCAL have individual PMTs located on the modules. All four detectors are segmented, which allows to associate the energy deposits to the tracks detected by the tracking system. The segmentation of the cells varies according to the distance from the beam pipe due to the different track density.

The most difficult identification is that of electrons. The rejection of a high background of charged pions is achieved using a longitudinal segmentation of the elec-

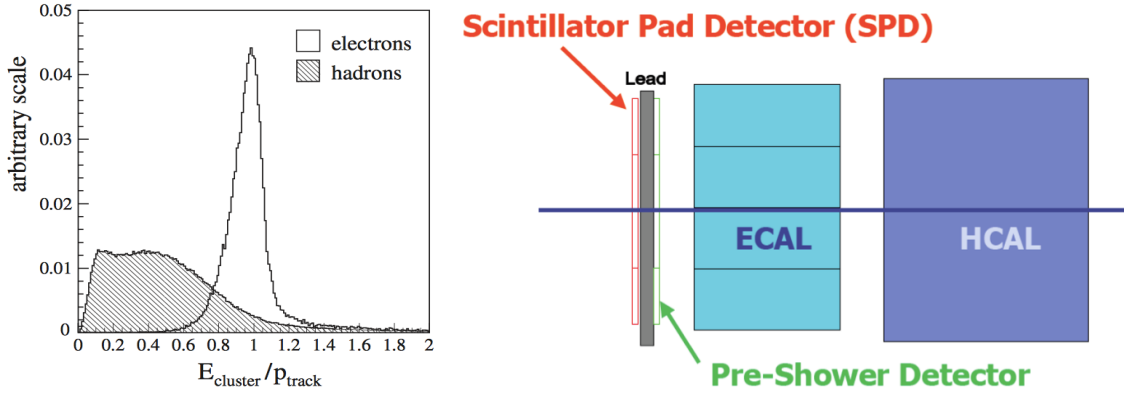


Figure 2.5: The ratio of the energy deposited in the ECAL and the particle momentum, which allows the separation between electrons and hadrons.

tromagnetic calorimeter which is provided by the PS detector added in front of the main electromagnetic calorimeter, ECAL. Electrons also have to be distinguished from high energy π^0 s. For this purpose the SPD calorimeter, detecting charged particles, is located in front of the PS and ECAL detectors. Figure 2.5 illustrates how the ratio between the energy detected in the ECAL and a particle's momentum allows the separation of electrons and hadrons.

In order to obtain the highest energy resolution the showers from high energy photons must be fully absorbed. For this reason the ECAL has a thickness of 25 radiation lengths and its resolution is measured to be [49]

$$\frac{\sigma_{\text{ECAL}}(E)}{E} = \frac{10\%}{\sqrt{E(\text{GeV})}} + 1\%, \quad (2.2)$$

which results in a mass resolution of $\sim 70 \text{ MeV}/c^2$ for B mesons and $\sim 8 \text{ MeV}/c^2$ for π^0 . The trigger requirements on the HCAL resolution do not depend on the containment of the hadron showers as much as for the ECAL, so, due to space limits, its thickness is only 5.6 interaction lengths and its resolution

$$\frac{\sigma_{\text{HCAL}}(E)}{E} = \frac{69\%}{\sqrt{E(\text{GeV})}} + 9\%. \quad (2.3)$$

600 2.5.1 Bremsstrahlung recovery for electrons

601 Bremsstrahlung is an electromagnetic radiation produced by charged particles that
 602 decelerate or deviate. Typically electrons produce Bremsstrahlung when deflected by
 603 atomic nuclei. The probability of emitting bremsstrahlung radiation is proportional
 604 to the inverse of the squared mass of the particle ($1/m^2$) and therefore it is relevant
 only for electrons. At LHC energies, if electrons radiate after the magnet, the

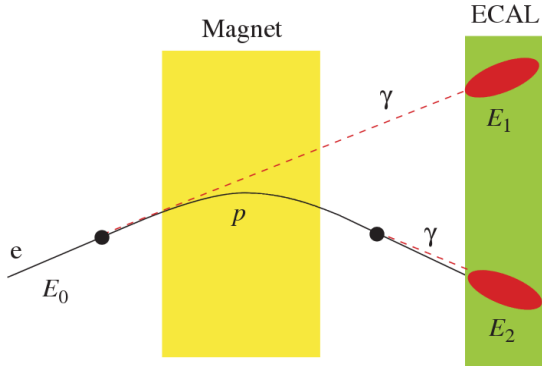


Figure 2.6: Schematic view of the bremsstrahlung recovery.

605
 606 photon will hit in the same calorimeter cells as the electron and the energy will be
 607 automatically recovered. However, if the photon is emitted before the magnet, the
 608 electron will be deflected by the magnetic field whereas the photon will continue
 609 on its initial trajectory, with its energy being deposited in a different part of the
 610 calorimeter. Missing this energy results in a poorer reconstructed invariant mass
 611 resolution, so it is desirable to recover these bremsstrahlung photons, when possible.
 612 A tool for bremsstrahlung recovery is available in the LHCb analysis software. This
 613 tool looks for other clusters in the calorimeter and, reconstructing the trajectory of
 614 the electron, checks if they may be associate with photons emitted by that. The
 615 photon energy is then added to the electron and its momentum is recalculated.
 616 Figure 2.6 displays a schematic view of the process. For more information see
 617 Ref. [53].

618 2.6 RICH

619 The two RICH detectors are a special feature of LHCb, as it is the only experiment
 620 at LHC including them. These detectors take advantage of the Cherenkov radiation
 621 produced by particles passing in a medium with velocity higher than the velocity
 622 of light in the medium. The Cherenkov light, as shown in Fig. 2.7, is produced in
 623 cones with a specific opening angle depending on the velocity of the particle. The
 624 relation between the angle and the particle velocity can be written as

$$\cos \theta = \frac{1}{\beta n}, \quad (2.4)$$

where $\beta = v/c$ and n is the refraction index of the medium.

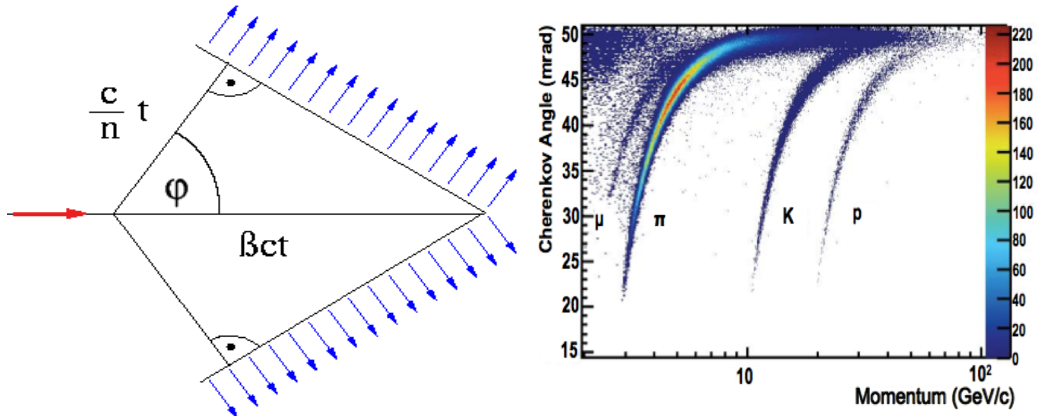


Figure 2.7: On the left a sketch of Cherenkov light emission and on the right the Cherenkov angle versus the particle momentum, where one can see that the study of the Cherenkov angle allows distinguish particles identities.

625

626 RICH 1 is located before the magnet in order to cover a larger angular accep-
 627 tance. Its purpose is to ensure particle identification over the momentum range
 628 $1 < p < 70 \text{ GeV}/c$. It uses two radiators: C_4F_{10} that covers the momentum range
 629 $5 - 70 \text{ GeV}/c$ and silica aerogel which covers $1 - 10 \text{ GeV}/c$. RICH 2 is positioned
 630 after the magnet and tracking stations and it identifies higher momentum particles
 631 from approximately $20 \text{ GeV}/c$ up to beyond $100 \text{ GeV}/c$ using CF_4 as a radiator.
 632 The Cherenkov light produced when charged particles travel through the radiators,
 633 is reflected and focused using mirrors, which are tilted so that the ring image is

634 reflected onto arrays of PMTs. The radius of the ring can be used to measure the
 635 opening angle of the Cherenkov cone because of the known geometry. The photo-
 636 detectors are located outside of the LHCb acceptance in order to reduce the amount
 637 of material that the particles have to traverse. Pattern recognition algorithms are
 638 then used to reconstruct the Cherenkov rings.

639 2.7 The muon system

640 It is essential for many of the key physics analyses in LHCb to be able to identify
 641 muons in decay final states. Muons are the most penetrating particles that can be
 642 detected at LHC experiments, so the muon chambers are the farthest sub-detectors
 643 from the interaction point. The muon system is formed by five stations (M1 -
 644 M5), the first one being located before the calorimeters in order to improve p_T
 645 measurements. The remaining four stations are behind the HCAL and are separated
 646 from each other and interleaved with 80 cm thick iron blocks, which absorb hadrons,
 647 electrons and photons to ensure that only muons reach the final muon station. A
 648 scheme of the muon system is shown in Fig. 2.8. Only muons with a minimum
 649 momentum of $10 \text{ GeV}/c$ traverse all of the five stations and, for positive identification
 650 of a muon, the trigger requires a signal in each of them. Each station has a detection
 651 efficiency of at least 95% and the detectors also provide position measurements.
 652 Since there is a larger particle flux towards the beam pipe, the stations are divided
 653 into four concentric rectangular regions (R1-R4), their size increasing according to
 654 the ratio $1 : 2 : 4 : 8$. This results in a similar channel occupancy over the four
 655 regions. All of the muon stations use Multi Wire Proportional Chambers (MWPC)
 656 except for the inner region of M1, where the particle flux is too high. In this region
 657 triple-GEM (Gas Electron Multiplier) detectors are used because of their better
 658 ageing properties as they have to withstand a rate up to 500 kHz cm^{-2} of charged
 659 particles. In these detectors particles traversing through the drift gap between the
 660 cathode and the first GEM foil produce ionisation electrons, which are then attracted
 661 by electric fields though all of the GEM foils and multiply. They then drift into the

662 anode inducing a signal on the pads. A gas mixture of Argon, CO_2 and CF_4 , is used
to give a time resolution better than 3 ns.

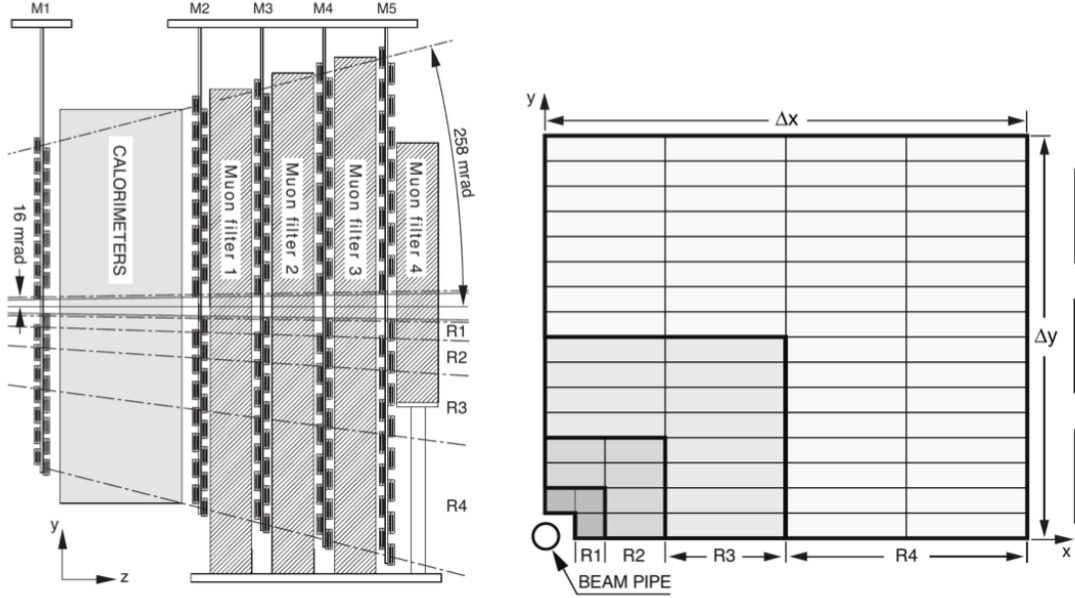


Figure 2.8: The LHCb muon system [49].

663

664 2.8 Particle identification

665 Particle identification (PID) is an important feature in LHCb and it is performed in
666 various ways. The electromagnetic calorimeters can distinguish between pions and
667 electron, the muon chambers identify muons and the RICH detectors can be used
668 to identify heavier charged particles as protons and kaons.

669 The RICH assigns an ID to a track calculating the global likelihood for the observed
670 distribution of hits being consistent with the expected distribution from various ID
671 hypothesis. The algorithm iterates through each track and recalculates the likeli-
672 hood when the track PID hypothesis is changed to that of an electron, muon, kaon
673 or proton. For electrons and muons additional information from the calorimeter
674 and muon systems is also used. The hypothesis which maximises the likelihood is
675 assigned to the track.

676 To quantify the quality of the ID the pion hypothesis is used as a reference point
 677 and the probability of a specific ID is given in terms of Log-Likelihood difference
 678 between the given ID hypothesis and the pion one. This variable is called Delta
 679 Log-Likelihood (DLL) and denoted with “PID”. For example:

$$\text{PID}_K = \text{DLL}_{K-\pi} = \log(\mathcal{L}_K) - \log(\mathcal{L}_\pi) \quad (2.5)$$

680 quantifies the probability of a particle being a kaon rather than a pion. Figure 2.9
 681 shows the efficiency of correctly identifying and mis-identifying kaons and protons as
 682 a function of the measured momentum of the particle. For kaons the efficiency drops
 683 at momenta below 10 GeV, where they fall below threshold for the gas radiators.
 684 The DLL cuts enable LHCb physics analyses to distinguish between kinematically
 685 similar decays with different final states, such as B^0 and B_s^0 mesons decaying into
 686 two hadrons. Figure 2.10 illustrates the power of particle identification, showing
 687 how the application of DLL cuts can be used to isolate $B^0 \rightarrow \pi^+\pi^-$ decays from
 other two-body B decays. Particularly important in LHCb is the identification of

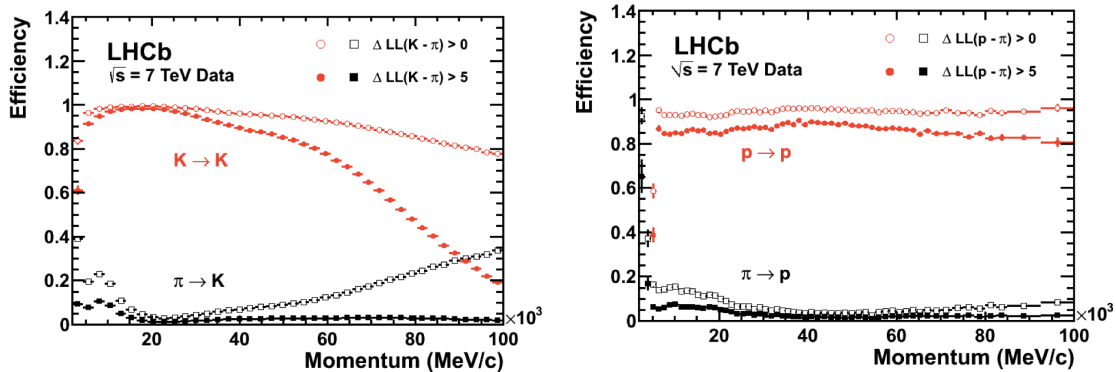


Figure 2.9: Particle Identification performances for kaons (left) and protons (right) as a function of the measured momentum of the particles.

688
 689 muons, which is quantified using two different variables: the DLL_μ and in addition
 690 the `isMuon` variable. The latter is a boolean variable determined by defining a ‘field
 691 of interest’ around a track trajectory extrapolated through the muon chambers.
 692 The variable is set to true if hits in multiple muon stations are found in the field of
 693 interest.

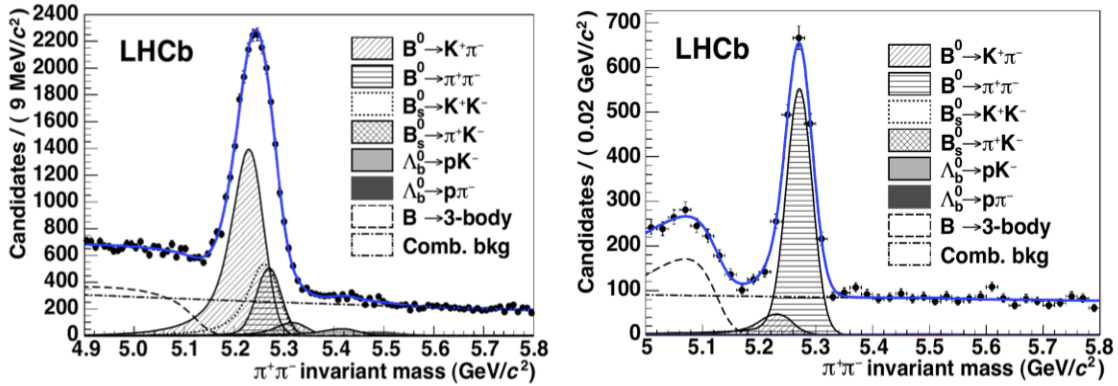


Figure 2.10: Invariant mass peak of the $B^0 \rightarrow \pi^+\pi^-$ decay before (left) and after (right) the application of PID requirements.

694 2.8.1 PID calibration

695 In order to be able to calculate detection efficiencies a data-driven method was
 696 developed. The calibration software is referred to as `PIDCalib` package [54]. This
 697 tool uses decays where final particles can be identified thanks to their kinematic
 698 properties. For example the $K_s^0 \rightarrow \pi^+\pi^-$ decay has a clear signature with a displaced
 699 vertex and can be easily singled out from other decays and used to test pion ID
 700 efficiency. The narrow peaks of the $J/\psi \rightarrow \mu^+\mu^-$ and $J/\psi \rightarrow e^+e^-$ decays allow to
 701 calibrate muon and electron efficiencies. A “tag-and-probe” method is used in this
 702 case, where only one of the two leptonic tracks is reconstructed requiring the correct
 703 identity and the other one is used to probe the PID efficiency. Finally, $\phi \rightarrow KK$
 704 samples and $D^{*+} \rightarrow D(\rightarrow K^-\pi^+)\pi^+$ decays, where the D^{*+} is used to tag the decay,
 705 are used to test the kaon efficiency. In all cases the residual background is subtracted
 706 using the $s\mathcal{P}$ lot technique [55].

707 2.9 Trigger and software

708 The LHCb trigger system [56] consists of a hardware stage, L0, based on information
 709 from the calorimeters and muon system, followed by a software stage, the High-
 710 Level Trigger (HLT), which applies a full reconstruction of the events. To increase

711 performances the HLT is further split into two stages, HLT1 and HLT2. The HLT1
 712 phase happens in real time and saves data in local disks while the HLT2 phase uses
 713 the resources available during periods with no beam. The event selected by the
 714 HLT2 stage are then saved for offline analysis. Figure 2.11 shows a scheme of the
 715 trigger system. The bunch crossing frequency is 40 MHz, which corresponds to an
 716 instantaneous luminosity of $2 \cdot 10^{32} \text{ cm}^{-2}\text{s}^{-1}$ for LHCb. About 15% of the total
 717 number of $b\bar{b}$ pairs produced will contain at least one B meson with all of its decay
 718 products within the detector acceptance. This rate needs to be reduced down to
 about 2 kHz at which the events can be written to disk.

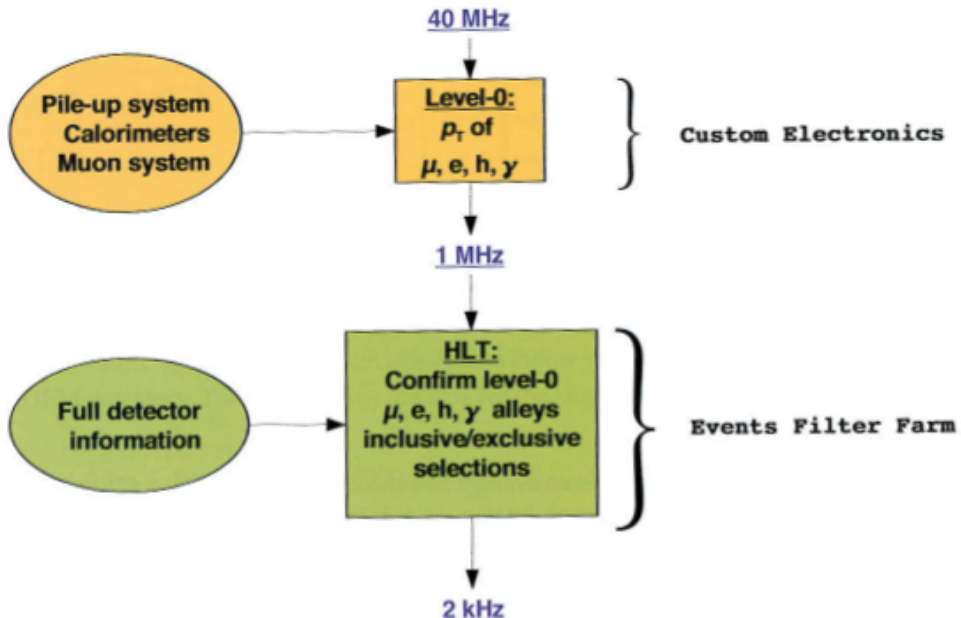


Figure 2.11: Scheme of the LHCb trigger system [49].

719

720 The L0 trigger reduces the rate of visible interactions from 10 MHz to 1 MHz.
 721 Due to the heavy mass of B mesons, they often produce particles with high p_T or
 722 E_T . Therefore the trigger selects events with large E_T deposits in the calorimeter
 723 or high p_T muons. The event is classified as L0Muon if it was triggered due to
 724 information for the muon detector, while the information from the calorimeters is
 725 used to divide the events in 5 categories: L0Photon, L0Electron, L0LocalPion,
 726 L0GlobalPion, L0Hadron. The PS detector information is converted to a photon
 727 flag (PS && !SPD) or an electron flag (PS && SPD). The “local” label of the L0Pion

728 trigger refers to π^0 reconstructed through their $\gamma\gamma$ decay, where the two photons fall
729 in the same ECAL element, they are labelled “global” otherwise. The first four
730 calorimeter triggers require energy clusters in the ECAL, while L0Hadron requires
731 clusters also in the HCAL. The HLT1 uses information from the VELO and trackers
732 performing a partial reconstruction of the event and reduces the rate to 2 kHz by
733 adding requirements of the IP and χ^2 of tracks. Finally, the HLT2 involves a full
734 reconstruction of the event and includes many “lines” designed to select specific
735 decay structures.

736 LHCb also developed an extended simulation software in order to reconstruct ef-
737 ficiencies and signal shapes. In the simulation, pp collisions are generated using
738 PYTHIA8 [57, 58] with a specific LHCb configuration [59]. Decays of hadronic par-
739 ticles are described by EVTGEN [60], and final state radiation is generated using
740 PHOTOS [61]. Finally, the interaction of the generated particles with the detec-
741 tor and its response are implemented using the GEANT4 toolkit [62] as described
742 in Ref. [63]. For this analysis in this thesis, the ROOT framework [64] is used to
743 analyse data and the RooFit package to perform maximum likelihood fits. A multi-
744 variate analysis is also performed based on the NeuroBayes package [65, 66], which
745 provides a framework for neural network training.

746 2.10 Kinematical fits

747 The resolution of key variables, such as the measured invariant mass of decaying
748 particles, can be improved by imposing constraints to the measured quantities to
749 remove redundant degrees of freedom. The four-momentum conservation can be
750 ensured at each vertex and the origin and decay vertices of a particle are related via
751 the momentum of the particle. Furthermore, additional constraints can be imposed
752 due to a particular decay hypothesis such as the known invariant masses of final and
753 intermediate particles. In order to do this the `DecayTreeFitter` tool was developed
754 by the BaBar experiment and later used by LHCb [67]. The algorithm takes a

complete decay chain and parameterises it in terms of vertex positions, decay lengths and momentum parameters. Then these parameters are fit simultaneously, taking into account the relevant constraints, including the information from photons. To perform the fit efficiently a Kalman filter is used. Figure 2.12 illustrates the effect of the application of the kinematical fit on the 4-body invariant mass of the final daughters of the $\Lambda_b^0 \rightarrow J/\psi \Lambda$ decay. The resolution in this case improves by over a factor of 2. Furthermore, the χ^2 from the kinematic fit can be used to quantify the likelihood of a specific decay structure, which helps to separate candidates where random particles from the event have been added to the decay tree or where one or more particles is not reconstructed or mis-identified.

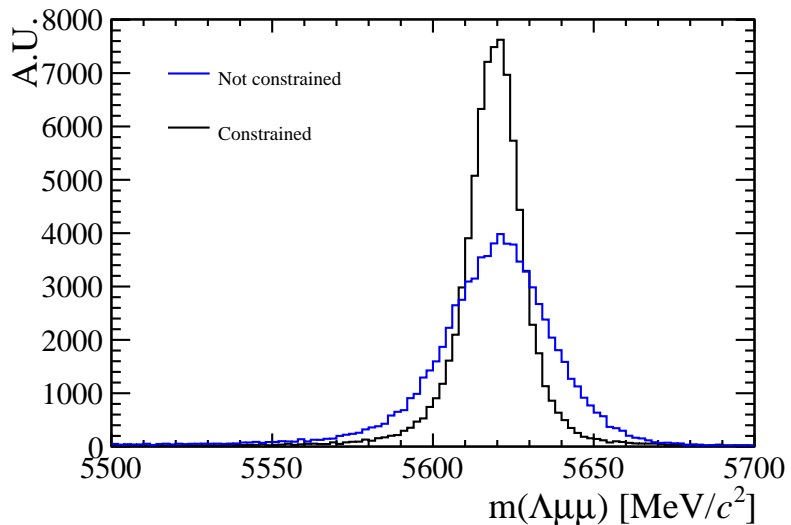


Figure 2.12: Invariant mass of the final daughters of simulated $\Lambda_b^0 \rightarrow J/\psi \Lambda$ decays calculated with and without constraints using the `DecayTreeFitter` tool.

764

2.11 Validation of hadronic processes in the simulation

Particle-antiparticle asymmetries are of major interest for LHCb and detection efficiencies are usually obtained from simulation. It is therefore important, in order to limit systematic uncertainties, to have a model that parametrises correctly the cross sections of particles and antiparticles or at least their ratio.

770 The LHCb simulation software propagates particles through the detector using the
771 GEANT4 toolkit [49]. This offers a variety of models for physics processes over a
772 wide range of energies for both electromagnetic and strong interactions. Given a
773 combination of projectile, target and energy there can be several models applicable
774 with different reliability and computational costs. GEANT4 provides a number of
775 pre-packaged physics lists each representing complete and consistent sets of models
776 chosen to be appropriate for a given use case. In LHCb mainly two hadronic physics
777 lists are considered:

- 778 • **LHEP** (Low and High Energy Parametrisation): based on a parametrised
779 modelling of all hadronic interactions for all particles. This list combines
780 the High Energy Parametrised model (HEP) and the low energy one (LEP).
781 There is a sharp switch from the low to the high energy model at 25 GeV.
782 The modelling of elastic scattering off a nucleus and of nuclear capture also
783 proceeds via parametrised models.
- 784 • **FTFP_BERT**: includes the following models:
- 785 – Bertini cascade model (BERT) [68], which simulates the intra-nuclear cas-
786 cade, followed by pre-equilibrium and evaporation phases of the residual
787 nucleus, for protons, neutrons, pions and kaons interaction with nuclei
788 at kinetic energies below 9.9 GeV. The Bertini model produces more
789 secondary neutrons and protons than the LEP model, yielding a better
790 agreement with experiment data.
- 791 – FTFP model, which implements high energy inelastic scattering of hadrons
792 by nuclei using the FRITIOF model [69]. The change between the two
793 models happens with a linear shift from BERT to FTF that starts at 4
794 GeV and ends at 5 GeV.

795 Figure 2.13 summarises the composition of the different models.

When two models overlap in an energy interval the choice of the model for each interaction is made using a random number: the probability to select each model varies linearly from 0 to 100% over the overlap range. Because of the differences of the two models in the overlap region, unphysical discontinuities can be produced as a function of energy.

2.11.1 Geometry and interaction probability

The results presented in the following sections are produced using the version v45r0 of the full LHCb framework for simulation, Gauss [63], interfaced to GEANT4 v95r2p1. A simple geometry setup is used in order to be able to calculate in a clean way the interaction cross sections in a specific material. This is constituted by a series of rectangular boxes filled with the most relevant materials for LHCb: Aluminium, Silicon and Beryllium. For each material three boxes are defined with different thicknesses (1mm, 10mm, 50mm). These values are chosen to represent a ballpark estimation of the LHCb interaction length.

The simplest quantity available to extract the cross section is the interaction probability (P_{int}), defined as:

$$P_{int} = \frac{N_{int}}{N_{tot}}, \quad (2.6)$$

where N_{int} is the number of particles which interacted in the material and N_{tot} is the number of generated particles. As GEANT4 provides an ID for the end process of a

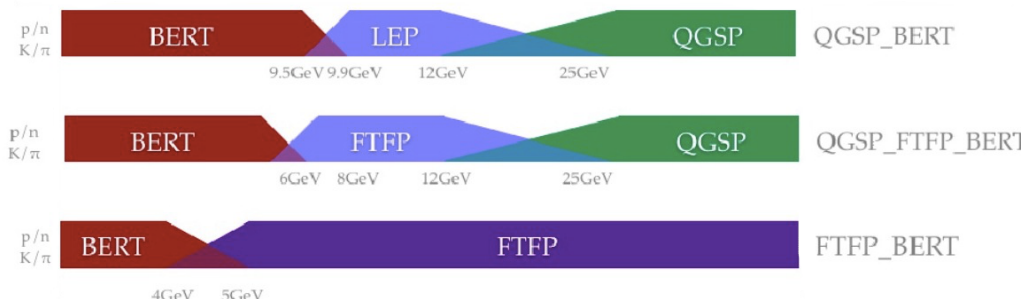


Figure 2.13: Diagram of LHEP, FTFP_BERT and QGSP_BERT models composition as a function of energy.

815 particle (e.g. 121 for inelastic interaction, 111 for elastic, 201 for decay) it is possible
816 to distinguish the inelastic and elastic probabilities of interaction and therefore cross
817 sections.

818 To compare simulation and data the cross section and P_{int} are linked by the following
819 formula valid for thin layers:

$$\sigma_{int} = \frac{A}{\rho N_A \Delta x} \cdot P_{int}, \quad (2.7)$$

820 where ρ is the density of the material and A is its mass number, Δx is the thickness
821 of the considered layer and N_A is the Avogadro number.

822 2.11.2 PDG prediction

In the PDG book [1] cross sections of protons and neutrons are parametrised as:

$$\sigma_{tot}^{ab} = Z^{ab} + B^{ab} \log^2(s/s_M) + Y_1^{ab}(s_M/s)^{\eta_1} - Y_2^{ab}(s_M/s)^{\eta_2}, \quad (2.8)$$

$$\sigma_{tot}^{\bar{a}\bar{b}} = Z^{ab} + B^{ab} \log^2(s/s_M) + Y_1^{ab}(s_M/s)^{\eta_1} + Y_2^{ab}(s_M/s)^{\eta_2}, \quad (2.9)$$

823 where $s_M = (m_a + m_b + M)^2$ and $B^{ab} = \lambda \pi (\frac{\hbar c}{M})^2$. Some of the constants in these
824 equations are universal and valid for any kind of collision: $M = 2.15$, $\eta_1 = 0.462$, η_2
825 = 0.551, $\lambda = 1$ (for p, n and γ) and 1.63 (for d). The other ones are characteristic
826 of each type of collision and are listed in Tab. 2.11.2. In these formulae the particle-
827 antiparticle asymmetry arises from the last term which has opposite sign in the
828 two equations. This term becomes less and less important with increasing energies.
829 Therefore a net asymmetry is found at low energies, while the cross sections tend
830 to a common point at high energy and continue increasing logarithmically.

2.11.3 Validation results

This section reports particle and antiparticle cross sections and their ratios compared where available with PDG predictions and with data from the COMPASS experiment [70]. Figure 2.14 shows the probability of interaction for protons and anti-protons in 1mm of Aluminium using the FTFP_BERT and LHEP models compared with COMPASS data and Fig. 2.15 shows the ratios of $\sigma_{\bar{p}}^{tot}/\sigma_p^{tot}$ together with the PDG prediction. A difference of 40% is found between the two considered models for 1 GeV incoming anti-protons. This difference becomes negligible at higher energies. The discrepancies between the two physics lists for kaons and pions are of a few percents (2-3%) and usually constant with the energy. From the comparison with data and PDG predictions it can be qualitatively concluded that the FTFP_BERT model gives a better description of hadronic interactions at low energies, while both models give good results at high energy, above ~ 10 GeV.

The tool developed for this studies is not limited to cross-sections but can also give information on other simulated quantities: as an example Fig. 2.11.3 shows a comparison between the types of particles generated in inelastic collisions of protons and anti-protons into Aluminium using different models. Different physics lists can give very different results. For example the LHEP model does not produce photons in inelastic collisions. However, it is difficult to use these quantities for validation as there is no data available for comparison.

852

Proj / Targ	Z^{ab}	Y_1^{ab}	Y_2^{ab}
$\bar{p}, p / p$	34.71	12.72	7.35
π^\pm / p	19.02	9.22	1.75
K^\pm / p	16.56	4.02	3.39
K^\pm / n	16.49	3.44	1.82
$\bar{p}, p / n$	35.00	12.19	6.62

Table 2.1: Values for the constants Z^{ab} , Y_1^{ab} and Y_2^{ab} [1], which parametrise hadronic cross sections.

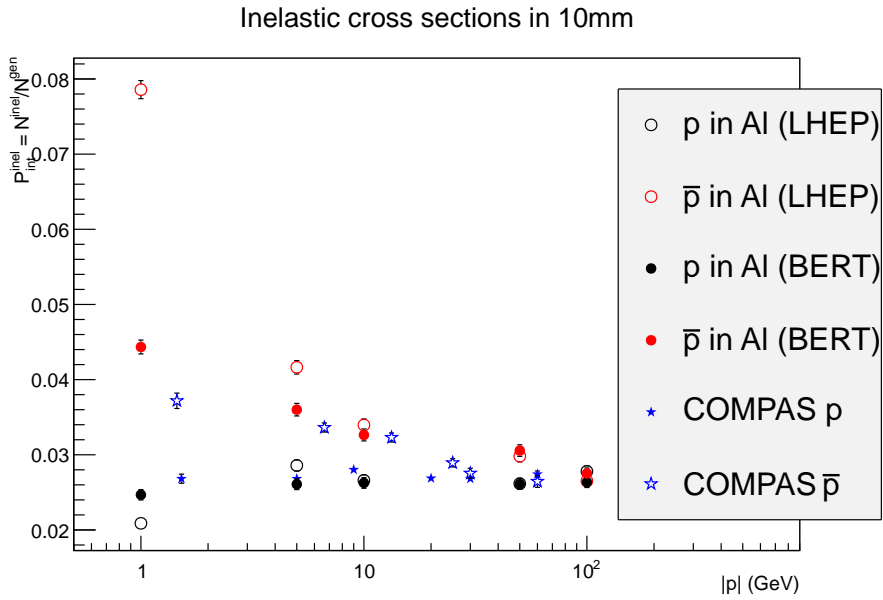


Figure 2.14: Probability of interaction for protons and anti-protons in Aluminium as a function of the projectile momentum. Two physics lists are used to generate events that can be compared with data from the COMPASS experiment.

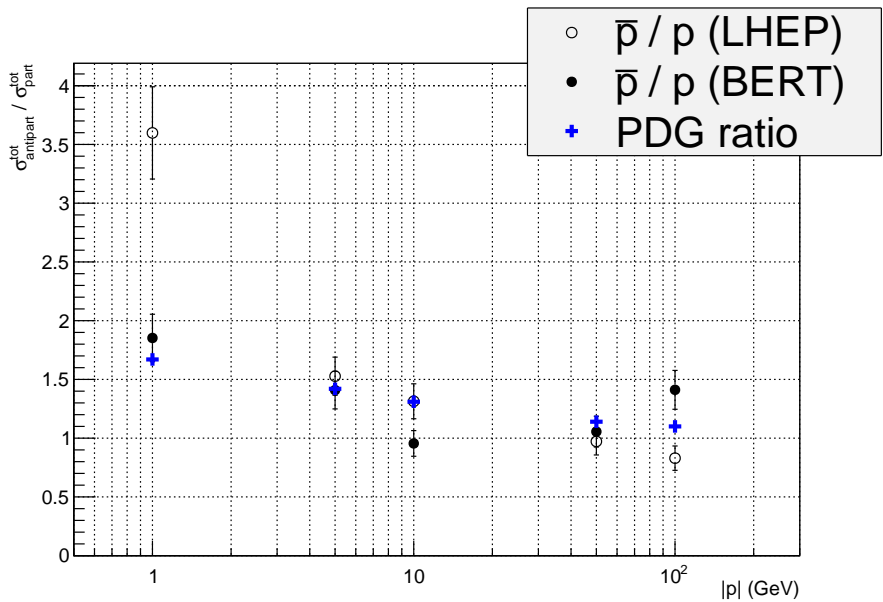


Figure 2.15: Ratio of antiproton over proton total interaction cross section as a function of energy compared with PDG predictions.

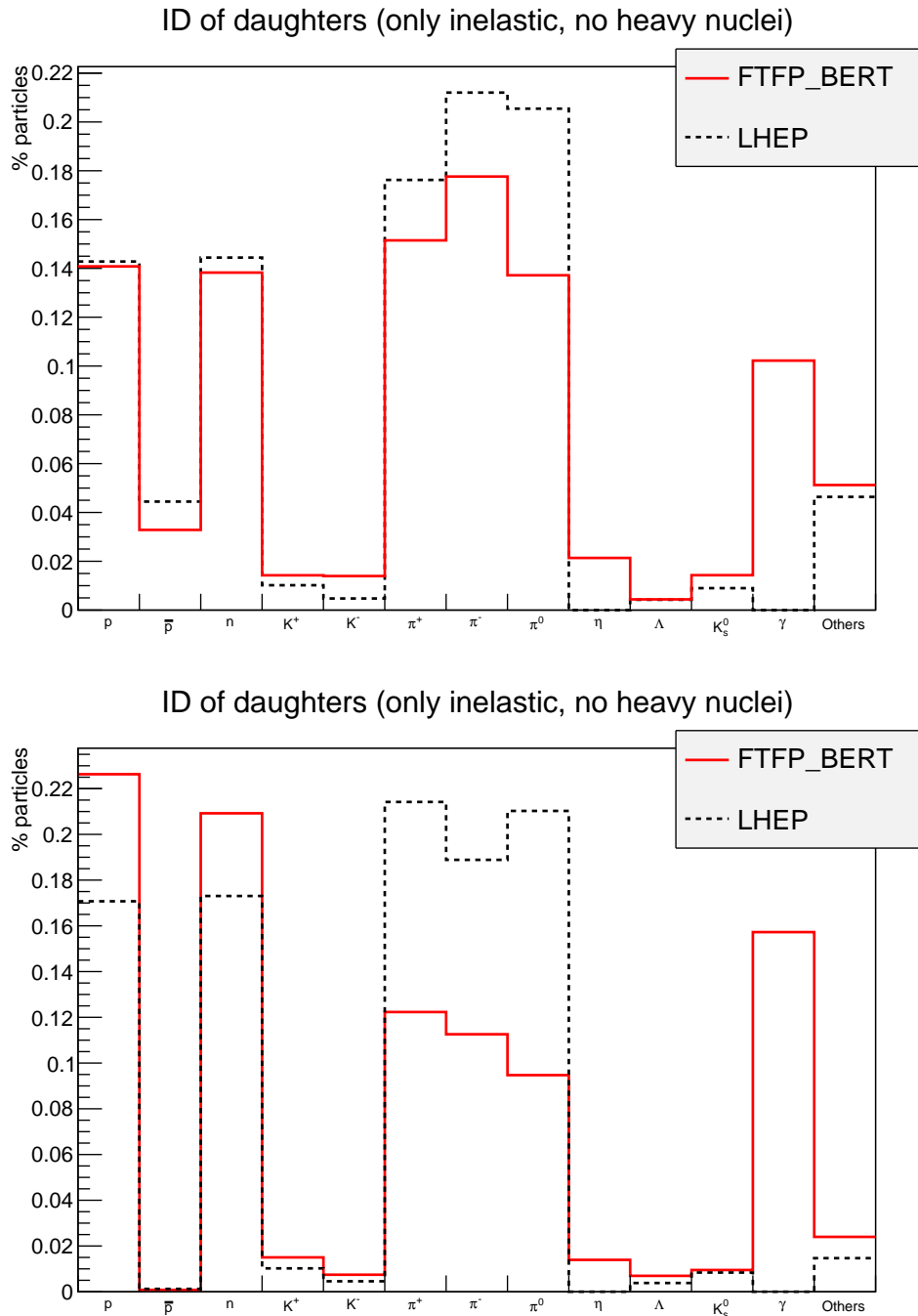


Figure 2.16: Composition of secondary particles produced in 100 GeV protons (top) and anti-protons (bottom) collisions in 1 mm Aluminium.

853 2.12 Material budget studies

854 It is important for many analysis to be aware of the material budget of the detector,
 855 for example to estimate the amount of multiple scattering. In GEANT4 particles
 856 are propagated in steps through the detector and for each step the framework anal-
 857 yses the geometry to understand in what material the particle is and modifies its
 858 trajectory accordingly. A tool was developed where neutrinos are used as probes to
 859 scan the detector summing the radiation length seen at each step up to a certain
 860 points. Neutrinos are used as they do not bend in magnetic field and do not interact
 861 with the detector. Thin air planes are inserted after each sub-detector. When these
 862 are traversed by the neutrinos the information about the cumulated radiation and
 863 interaction length is saved. In this way it is possible to obtain maps of the detector
 864 as the one shown in Fig. 2.17. Finally, Fig. 2.18 shows the average radiation length
 865 as a function of the distance from the interaction point.

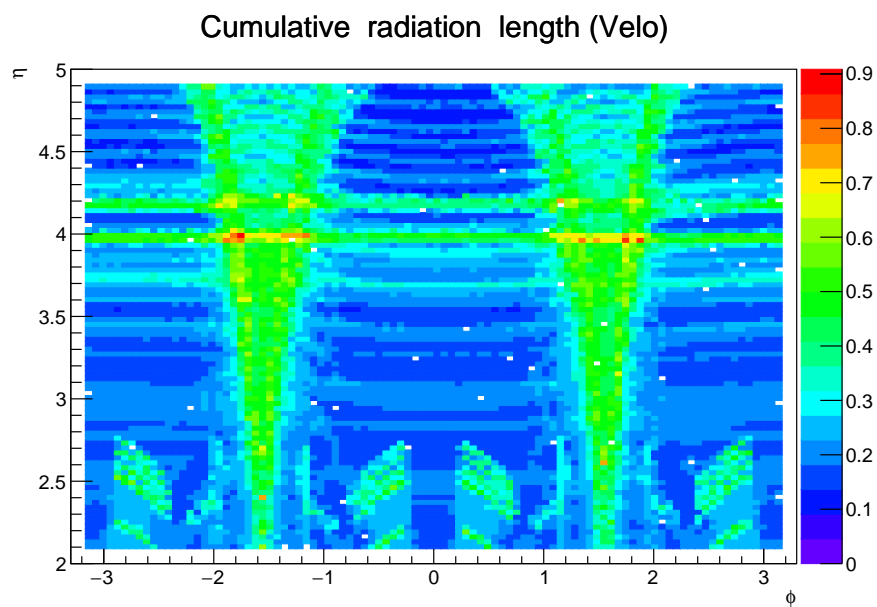


Figure 2.17: Map of cumulative radiation length traversed by a particle starting from the interaction point up to the end of the VeLo.

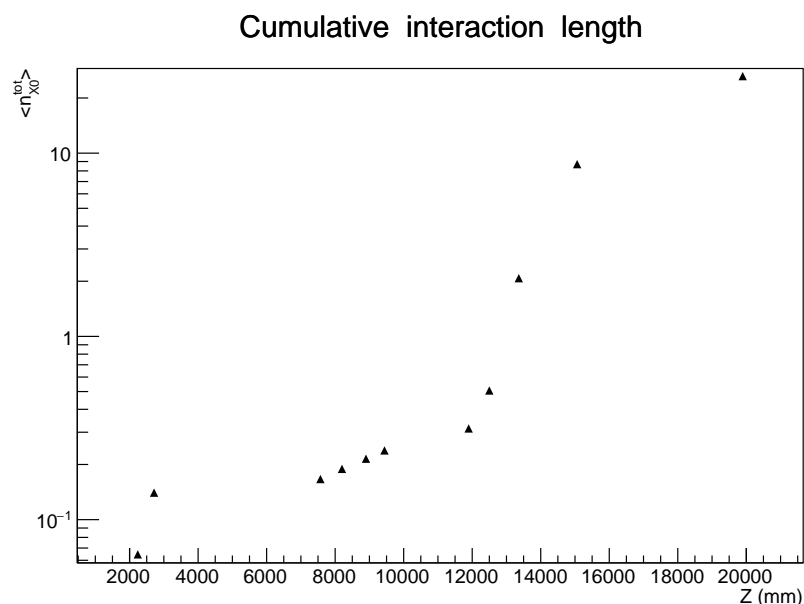


Figure 2.18: Average cumulative radiation length as a function of the horizontal distance from the interaction point. Each considered point corresponds to the end of a sub-detector: VeLo, RICH1, RICH2, tracking stations, ECAL and HCAL and muon detector.

867

868

REFERENCES

869

- 870 [1] **Particle Data Group** Collaboration, K. Olive et al., *Review of Particle*
871 *Physics, Chin.Phys.* **C38** (2014) 090001.
- 872 [2] L. Susskind, *Dynamics of Spontaneous Symmetry Breaking in the*
873 *Weinberg-Salam Theory, Phys.Rev.* **D20** (1979) 2619–2625.
- 874 [3] S. Glashow, *Partial Symmetries of Weak Interactions, Nucl.Phys.* **22** (1961)
875 579–588.
- 876 [4] **LHCb** Collaboration, R. Aaij et al., *Observation of the resonant character of*
877 *the $Z(4430)^-$ state, Phys. Rev. Lett.* **112** (2014), no. 22 222002,
878 [[arXiv:1404.1903](#)].
- 879 [5] **LHCb** Collaboration, R. Aaij et al., *Observation of $J/\psi p$ resonances*
880 *consistent with pentaquark states in $\Lambda_b^0 \rightarrow J/\psi K^- p$ decays,*
881 [[arXiv:1507.03414](#)].
- 882 [6] C. Wu, E. Ambler, R. Hayward, D. Hopps, and R. Hudson, *Experimental*
883 *Test of Parity Conservation in Beta Decay, Phys.Rev.* **105** (1957) 1413–1414.
- 884 [7] F. Strocchi, *Spontaneous Symmetry Breaking in Local Gauge Quantum Field*
885 *Theory: The Higgs Mechanism, Commun.Math.Phys.* **56** (1977) 57.
- 886 [8] J. Charles, O. Deschamps, S. Descotes-Genon, H. Lacker, A. Menzel, et al.,
887 *Current status of the Standard Model CKM fit and constraints on $\Delta F = 2$*
888 *New Physics, Phys.Rev.* **D91** (2015), no. 7 073007, [[arXiv:1501.05013](#)].
- 889 [9] F. Zwicky, *Spectral displacement of extra galactic nebulae, Helv.Phys.Acta* **6**
890 (1933) 110–127.

- 891 [10] M. Gavela and Hernandez, *Standard model CP violation and baryon
892 asymmetry*, *Mod.Phys.Lett.* **A9** (1994) 795–810, [[hep-ph/9312215](#)].
- 893 [11] M. Maltoni, *Status of three-neutrino oscillations*, *PoS EPS-HEP2011* (2011)
894 090.
- 895 [12] B. T. Cleveland, T. Daily, R. Davis, Jr., J. R. Distel, K. Lande, C. K. Lee,
896 P. S. Wildenhain, and J. Ullman, *Measurement of the solar electron neutrino
897 flux with the Homestake chlorine detector*, *Astrophys. J.* **496** (1998) 505–526.
- 898 [13] **Super-Kamiokande** Collaboration, Y. Fukuda et al., *Evidence for
899 oscillation of atmospheric neutrinos*, *Phys. Rev. Lett.* **81** (1998) 1562–1567,
900 [[hep-ex/9807003](#)].
- 901 [14] **KamLAND** Collaboration, K. Eguchi et al., *First results from KamLAND:
902 Evidence for reactor anti-neutrino disappearance*, *Phys. Rev. Lett.* **90** (2003)
903 021802, [[hep-ex/0212021](#)].
- 904 [15] J. L. Feng, *Naturalness and the Status of Supersymmetry*,
905 *Ann.Rev.Nucl.Part.Sci.* **63** (2013) 351–382, [[arXiv:1302.6587](#)].
- 906 [16] **ATLAS** Collaboration, G. Aad et al., *Observation of a new particle in the
907 search for the Standard Model Higgs boson with the ATLAS detector at the
908 LHC*, *Phys. Lett.* **B716** (2012) 1–29, [[arXiv:1207.7214](#)].
- 909 [17] P. Fayet and S. Ferrara, *Supersymmetry*, *Phys.Rept.* **32** (1977) 249–334.
- 910 [18] L. Randall and R. Sundrum, *A Large mass hierarchy from a small extra
911 dimension*, *Phys.Rev.Lett.* **83** (1999) 3370–3373, [[hep-ph/9905221](#)].
- 912 [19] G. Isidori and D. M. Straub, *Minimal Flavour Violation and Beyond*,
913 *Eur.Phys.J.* **C72** (2012) 2103, [[arXiv:1202.0464](#)].
- 914 [20] A. J. Buras, *Minimal flavor violation*, *Acta Phys.Polon.* **B34** (2003)
915 5615–5668, [[hep-ph/0310208](#)].
- 916 [21] T. Blake, T. Gershon, and G. Hiller, *Rare b hadron decays at the LHC*,
917 *Ann.Rev.Nucl.Part.Sci.* **65** (2015) 8007, [[arXiv:1501.03309](#)].
- 918 [22] A. J. Buras, D. Buttazzo, J. Girrbach-Noe, and R. Knegjens, *Can we reach
919 the Zeptouniverse with rare K and $B_{s,d}$ decays?*, *JHEP* **1411** (2014) 121,
920 [[arXiv:1408.0728](#)].
- 921 [23] G. Hiller and M. Schmaltz, *R_K and future $b \rightarrow s\ell\ell$ physics beyond the standard
922 model opportunities*, *Phys.Rev.* **D90** (2014) 054014, [[arXiv:1408.1627](#)].
- 923 [24] K. G. Chetyrkin, M. Misiak, and M. Munz, *Weak radiative B meson decay
924 beyond leading logarithms*, *Phys.Lett.* **B400** (1997) 206–219,
925 [[hep-ph/9612313](#)].

- [25] G. Buchalla, A. J. Buras, and M. E. Lautenbacher, *Weak decays beyond leading logarithms*, *Rev.Mod.Phys.* **68** (1996) 1125–1144, [[hep-ph/9512380](#)].
- [26] A. J. Buras, *Weak Hamiltonian, CP violation and rare decays*, [hep-ph/9806471](#).
- [27] M. Della Morte, J. Heitger, H. Simma, and R. Sommer, *Non-perturbative Heavy Quark Effective Theory: An application to semi-leptonic B-decays*, *Nucl.Part.Phys.Proc.* **261-262** (2015) 368–377, [[arXiv:1501.03328](#)].
- [28] C. W. Bauer, S. Fleming, D. Pirjol, and I. W. Stewart, *An Effective field theory for collinear and soft gluons: Heavy to light decays*, *Phys.Rev.* **D63** (2001) 114020, [[hep-ph/0011336](#)].
- [29] A. Khodjamirian, T. Mannel, A. Pivovarov, and Y.-M. Wang, *Charm-loop effect in $B \rightarrow K^{(*)}\ell^+\ell^-$ and $B \rightarrow K^*\gamma$* , *JHEP* **1009** (2010) 089, [[arXiv:1006.4945](#)].
- [30] **LHCb** Collaboration, R. Aaij et al., *Observation of a resonance in $B^+ \rightarrow K^+\mu^+\mu^-$ decays at low recoil*, *Phys. Rev. Lett.* **111** (2013) 112003, [[arXiv:1307.7595](#)].
- [31] C. Bobeth, M. Gorbahn, T. Hermann, M. Misiak, E. Stamou, et al., *$B_{s,d} \rightarrow l + l -$ in the Standard Model with Reduced Theoretical Uncertainty*, *Phys.Rev.Lett.* **112** (2014) 101801, [[arXiv:1311.0903](#)].
- [32] **CMS, LHCb** Collaboration, V. Khachatryan et al., *Observation of the rare $B_s^0 \rightarrow \mu^+\mu^-$ decay from the combined analysis of CMS and LHCb data*, *Nature* **522** (2015) 68–72, [[arXiv:1411.4413](#)].
- [33] **LHCb** Collaboration, R. Aaij et al., *Differential branching fractions and isospin asymmetry of $B \rightarrow K^{(*)}\mu^+\mu^-$ decays*, *JHEP* **06** (2014) 133, [[arXiv:1403.8044](#)].
- [34] **LHCb** Collaboration, R. Aaij et al., *Differential branching fraction and angular analysis of the decay $B_s^0 \rightarrow \phi\mu^+\mu^-$* , *JHEP* **07** (2013) 084, [[arXiv:1305.2168](#)].
- [35] **LHCb** Collaboration, R. Aaij et al., *Differential branching fraction and angular analysis of the decay $B^0 \rightarrow K^{*0}\mu^+\mu^-$* , *JHEP* **08** (2013) 131, [[arXiv:1304.6325](#)].
- [36] **LHCb** Collaboration, R. Aaij et al., *Differential branching fraction and angular analysis of $\Lambda_b^0 \rightarrow \Lambda\mu^+\mu^-$ decays*, *JHEP* **1506** (2015) 115, [[arXiv:1503.07138](#)].
- [37] **LHCb** Collaboration, R. Aaij et al., *Measurement of form-factor-independent observables in the decay $B^0 \rightarrow K^{*0}\mu^+\mu^-$* , *Phys. Rev. Lett.* **111** (2013) 191801, [[arXiv:1308.1707](#)].

- 963 [38] S. Descotes-Genon, J. Matias, and J. Virto, *Understanding the $B \rightarrow K^* \mu^+ \mu^-$ Anomaly*, *Phys. Rev.* **D88** (2013), no. 7 074002, [[arXiv:1307.5683](#)].
- 964
- 965 [39] **LHCb** Collaboration, R. Aaij et al., *Angular analysis of charged and neutral*
966 *$B \rightarrow K \mu^+ \mu^-$ decays*, *JHEP* **05** (2014) 082, [[arXiv:1403.8045](#)].
- 967 [40] **LHCb** Collaboration, R. Aaij et al., *Measurement of CP asymmetries in the*
968 *decays $B^0 \rightarrow K^{*0} \mu^+ \mu^-$ and $B^+ \rightarrow K^+ \mu^+ \mu^-$* , *JHEP* **1409** (2014) 177,
969 [[arXiv:1408.0978](#)].
- 970 [41] **LHCb** Collaboration, R. Aaij et al., *Measurement of the $B^0 \rightarrow K^{*0} e^+ e^-$*
971 *branching fraction at low dilepton mass*, *JHEP* **05** (2013) 159,
972 [[arXiv:1304.3035](#)].
- 973 [42] **LHCb** Collaboration, R. Aaij et al., *Angular analysis of the $B^0 \rightarrow K^{*0} e^+ e^-$*
974 *decay in the low- q^2 region*, *JHEP* **04** (Jan, 2015) 064. 18 p.
- 975 [43] **MEGA** Collaboration, M. Ahmed et al., *Search for the lepton family number*
976 *nonconserving decay $\mu u^+ \rightarrow e^+ \gamma$* , *Phys. Rev.* **D65** (2002) 112002,
977 [[hep-ex/0111030](#)].
- 978 [44] **SINDRUM** Collaboration, U. Bellgardt et al., *Search for the Decay*
979 *$\mu u^+ \rightarrow e^+ e^+ e^-$* , *Nucl. Phys.* **B299** (1988) 1.
- 980 [45] **LHCb** Collaboration, R. Aaij et al., *Search for the lepton-flavour-violating*
981 *decays $B_s^0 \rightarrow e^\pm \mu^\mp$ and $B^0 \rightarrow e^\pm \mu^\mp$* , *Phys. Rev. Lett.* **111** (2013) 141801,
982 [[arXiv:1307.4889](#)].
- 983 [46] **LHCb** Collaboration, R. Aaij et al., *Searches for violation of lepton flavour*
984 *and baryon number in tau lepton decays at LHCb*, *Phys. Lett.* **B724** (2013) 36,
985 [[arXiv:1304.4518](#)].
- 986 [47] W. J. Marciano, T. Mori, and J. M. Roney, *Charged Lepton Flavor Violation*
987 *Experiments*, *Ann. Rev. Nucl. Part. Sci.* **58** (2008) 315–341.
- 988 [48] L. Evans, *The LHC machine*, *PoS EPS-HEP2009* (2009) 004.
- 989 [49] **LHCb** Collaboration, A. A. Alves Jr. et al., *The LHCb detector at the LHC*,
990 *JINST* **3** (2008) S08005.
- 991 [50] **LHCb** Collaboration, R. Aaij et al., *Measurement of $\sigma(pp \rightarrow b\bar{b}X)$ at*
992 *$\sqrt{s} = 7$ TeV in the forward region*, *Phys. Lett.* **B694** (2010) 209–216,
993 [[arXiv:1009.2731](#)].
- 994 [51] M. Adinolfi et al., *Performance of the LHCb RICH detector at the LHC*, *Eur.*
995 *Phys. J.* **C73** (2013) 2431, [[arXiv:1211.6759](#)].
- 996 [52] A. A. Alves Jr. et al., *Performance of the LHCb muon system*, *JINST* **8**
997 (2013) P02022, [[arXiv:1211.1346](#)].

- 998 [53] **LHCb** Collaboration, R. e. a. Aaij, *LHCb technical design report: Reoptimized detector design and performance*, CERN-LHCC-2003-030.
- 1000 [54] **LHCb** Collaboration, R. e. a. Aaij, *LHCb Detector Performance*, *Int. J. Mod. Phys. A* **30** (Dec, 2014) 1530022. 82 p.
- 1002 [55] M. Pivk and F. R. Le Diberder, *SPlot: A Statistical tool to unfold data distributions*, *Nucl.Instrum.Meth.* **A555** (2005) 356–369, [[physics/0402083](#)].
- 1004 [56] R. Aaij et al., *The LHCb trigger and its performance in 2011*, *JINST* **8** (2013) P04022, [[arXiv:1211.3055](#)].
- 1006 [57] T. Sjöstrand, S. Mrenna, and P. Skands, *PYTHIA 6.4 physics and manual*, *JHEP* **05** (2006) 026, [[hep-ph/0603175](#)].
- 1008 [58] T. Sjostrand, S. Mrenna, and P. Z. Skands, *A Brief Introduction to PYTHIA 8.1*, *Comput. Phys. Commun.* **178** (2008) 852–867, [[arXiv:0710.3820](#)].
- 1010 [59] I. Belyaev et al., *Handling of the generation of primary events in GAUSS, the LHCb simulation framework*, *Nuclear Science Symposium Conference Record (NSS/MIC)* IEEE (2010) 1155.
- 1013 [60] D. J. Lange, *The EvtGen particle decay simulation package*, *Nucl. Instrum. Meth.* **A462** (2001) 152–155.
- 1015 [61] P. Golonka and Z. Was, *PHOTOS Monte Carlo: a precision tool for QED corrections in Z and W decays*, *Eur.Phys.J.* **C45** (2006) 97–107, [[hep-ph/0506026](#)].
- 1018 [62] **Geant4 collaboration** Collaboration, J. Allison, K. Amako, J. Apostolakis, H. Araujo, P. Dubois, et al., *Geant4 developments and applications*, *IEEE Trans.Nucl.Sci.* **53** (2006) 270.
- 1021 [63] M. Clemencic et al., *The LHCb simulation application, GAUSS: design, evolution and experience*, *J. Phys. Conf. Ser.* **331** (2011) 032023.
- 1023 [64] R. Brun, F. Rademakers, and S. Panacek, *ROOT, an object oriented data analysis framework*, *Conf.Proc. C000917* (2000) 11–42.
- 1025 [65] M. Feindt and U. Kerzel, *The NeuroBayes neural network package*, *Nucl.Instrum.Meth.* **A559** (2006) 190–194.
- 1027 [66] M. Feindt, *A Neural Bayesian Estimator for Conditional Probability Densities*, [physics/0402093](#).
- 1029 [67] W. D. Hulsbergen, *Decay chain fitting with a Kalman filter*, *Nucl.Instrum.Meth.* **A552** (2005) 566–575, [[physics/0503191](#)].
- 1031 [68] H. W. Bertini, *Low-Energy Intranuclear Cascade Calculation*, *Phys. Rev.* **131** (1963) 1801–1821.

- 1033 [69] B. Andersson, G. Gustafson, and H. Pi, *The FRITIOF model for very*
1034 *high-energy hadronic collisions*, *Z. Phys.* **C57** (1993) 485–494.
- 1035 [70] **COMPASS** Collaboration, P. Abbon et al., *The COMPASS experiment at*
1036 *CERN*, *Nucl. Instrum. Meth.* **A577** (2007) 455–518, [[hep-ex/0703049](#)].
- 1037 [71] **LHCb** Collaboration, R. Aaij et al., *Determination of the quark coupling*
1038 *strength $|V_{ub}|$ using baryonic decays*, [arXiv:1504.01568](#).
- 1039 [72] A. Crivellin and S. Pokorski, *Can the differences in the determinations of*
1040 *V_{ub} and V_{cb} be explained by New Physics?*, *Phys. Rev. Lett.* **114** (2015),
1041 no. 1 011802, [[arXiv:1407.1320](#)].
- 1042 [73] W. Altmannshofer and D. M. Straub, *New physics in $b \rightarrow s$ transitions after*
1043 *LHC run 1*, [arXiv:1411.3161](#).

1044

APPENDIX A

1045

1046

Extra

1047

1048 A.0.1 Quantum Electrodynamics: an example of gauge field theory

1049 *Possible addition around Sec. 1.1.*

1050 The EM theory results from requiring the fermion Lagrangian to be invariant un-
1051 der local gauge transformations. The electron and positron free fermionic fields
1052 are defined as $\psi(x)$ and $\bar{\psi}(x)$, where x is a relativistic four vector. A local gauge
1053 transformation can always be written as:

$$\psi(x) \rightarrow \psi(x') = e^i \alpha(x) \psi(x) \quad (\text{A.1})$$

1054 where $\alpha(x)$ can be any function of space and/or time. The free fermion Lagrangian,
1055 given by

$$\mathcal{L} = -i\bar{\psi}(x)\gamma^\mu \partial_\mu \psi(x) - m\bar{\psi}(x)\psi \quad (\text{A.2})$$

1056 is not invariant under such transformations. Greek indices denote space-time direc-
1057 tions and imply summation and γ^i are the Dirac matrices. If we apply the local
1058 gauge transformation and we subtract the initial Lagrangian we get a remaining
1059 term

$$\Delta\mathcal{L} = \mathcal{L}' - \mathcal{L} = -i\bar{\psi}\gamma^\mu\psi\partial_\mu\alpha(x) \quad (\text{A.3})$$

1060 In order to make the Lagrangian invariant we can introduce a vector field A , which
1061 transforms as described by Eq. A.4, to

$$A'_\mu = A_\mu - \frac{1}{e}\partial_\mu\alpha(x) \quad (\text{A.4})$$

1062 Redefining then the field derivative $D_\mu = \partial_\mu - ieA_\mu$, we obtain the invariant La-
1063 grangian:

$$\mathcal{L} = -i\bar{\psi}(x)\gamma^\mu D_\mu\psi(x) - m\bar{\psi}(x)\psi = -i\bar{\psi}(x)(\gamma^\mu\partial_\mu - m)\psi(x) + e\bar{\psi}\gamma^\mu\psi A_\mu \quad (\text{A.5})$$

1064 In this Lagrangian the first term describes the behaviours of a free fermion and the
1065 second term, $\bar{\psi}\gamma^\mu\psi A_\mu$, the electromagnetic interaction through the photon repre-
1066 sented by A_μ .

1067 A.1 Anomalies

1068 *Possible addition around Sec. 1.6.*

1069 Various anomalies were observed in the past years with respect to SM predictions.
1070 This section reports a brief review of these anomalies, limiting to B physics.

1071 The measurement of the CKM matrix elements V_{ub} and V_{cb} is vital for analysis in the
1072 flavour sector. Both these quantities can be measured using tree level transitions,
1073 which are assumed to be free from NP. Decays such as $B \rightarrow D^*\ell\nu$ are used to
1074 measure V_{cb} and $B \rightarrow \pi\ell\nu$ for V_{ub} as well as inclusive decays. Several measurements,
1075 mainly from BaBar and LHCb [71, ?], observe a discrepancy at 2σ level between
1076 the values found using the exclusive and inclusive approaches. This has recently
1077 increased to 3σ level due to improvements in form factor calculations [72]. NP can
1078 modify the values of the CKM matrix elements as described in Ref. [].

1079 Secondly a series of anomalies was found in recent LHCb measurements of semilep-
1080 tonic B decays. The branching ratios of the $B \rightarrow K\mu^+\mu^-$, $B \rightarrow K^{*0}\mu^+\mu^-$ and
1081 $B_s^0 \rightarrow \phi\mu^+\mu^-$ [33, 34, 35] are all found to be slightly below the predicted values. Al-
1082 though taken by itself each measurement does not present relevant discrepancies,
1083 the systematic deviation seems to indicate a more general picture. Angular analy-
1084 sis were also performed for these decays and, while most observables are found to
1085 agree with SM predictions, the measurement of the P'_5 observable in $B \rightarrow K^{*0}\mu^+\mu^-$

1086 resulted in a local 3.7σ deviation with respect to predictions []. At the same time
1087 the measurement of the R_K ratio, between the branching fractions of the $B^0 \rightarrow K^{*0}$
1088 $\mu^+\mu^-$ and $B^0 \rightarrow K^{*0} e^+e^-$ decays, showed a 2.6σ deviation from unity, indicating
1089 the possibility of a violation of lepton flavour universality. Authors of Ref. [73] per-
1090 formed a global fit taking into account of several measurements and found that a
1091 model with a NP component in C_9 is preferred with respect to the SM at 4.3σ level.
1092 Finally, one more discrepancy linked to this picture is the branching fraction of the
1093 $h \rightarrow \mu\tau$ decay, which is found to be different from zero at 2.4σ level.